Supporting Information

Room-Temperature Solution-Processed Spin Organic Light-Emitting Diodes Based on Chiral 2D Halide Perovskites

Lan-Sheng Yang, Chun-Yao Huang, Chin-An Hsu, Hao-Zhe Chiu, Pei-Hsuan Lo, Yu-Chiang Chao**

L.-S. Yang, C.-Y. Huang, C.-A. Hsu, H.-Z. Chiu, P.-H. Lo, Prof. Y.-C. Chao
Department of Physics
National Taiwan Normal University
Taipei 11677, Taiwan, R.O.C.
E-mail: s10365love@gmail.com, ycchao@ntnu.edu.tw.

Keywords: perovskite, circular dichroism, circularly polarized photoluminescence, magnetic field effect, dissymmetry factor

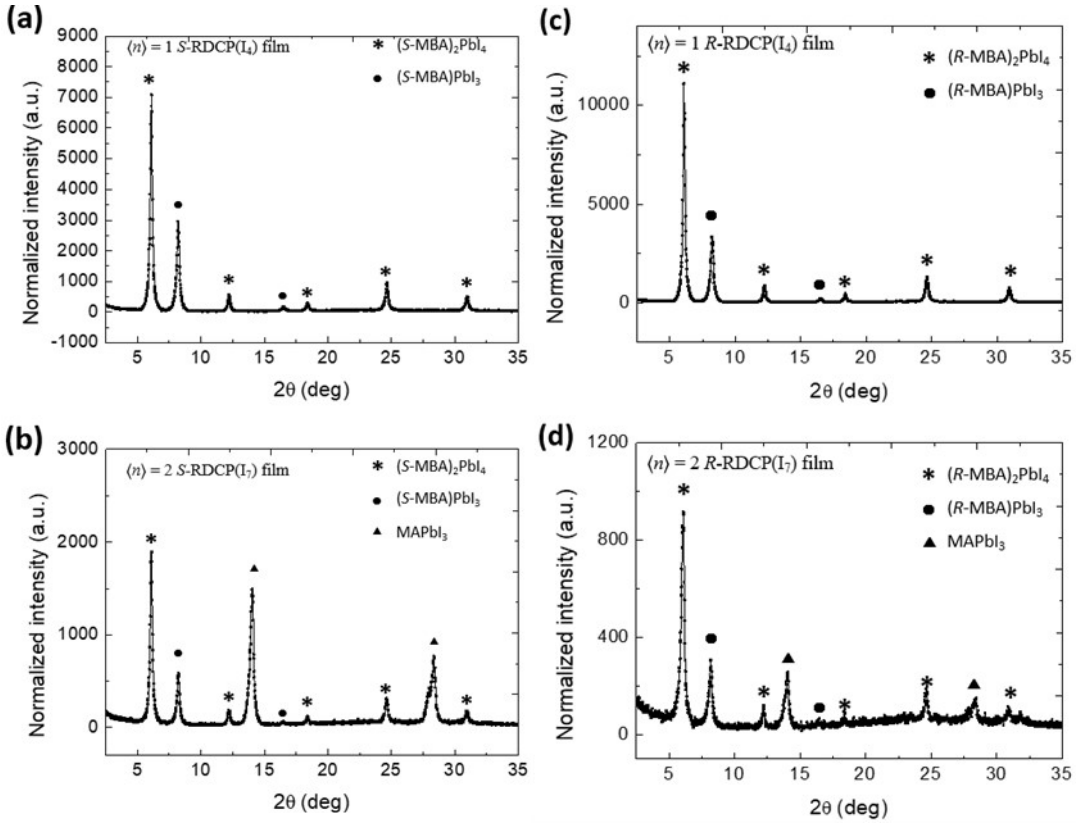

Figure S1 X-ray diffraction patterns of S-/*R*-RDCP films with (a) $\langle n \rangle = 1$ and (b) $\langle n \rangle = 2$.

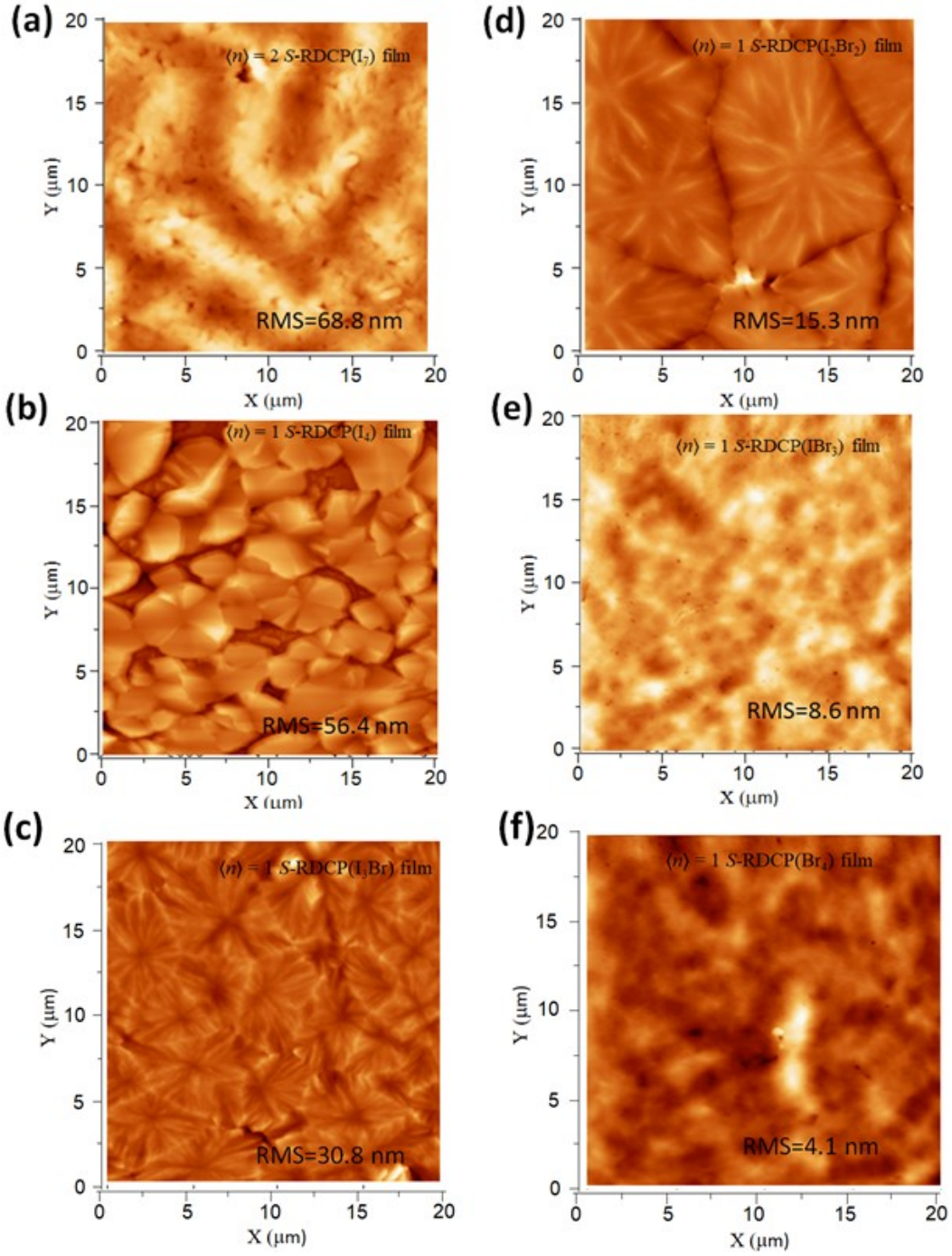

Figure S2 AFM images for (a) ⟨n⟩ = 2 S-RDCP(I_7) film, (b) ⟨n⟩ = 1 S-RDCP(I_4), (c) ⟨n⟩ = 1 S-RDCP(I_3Br), (d) ⟨n⟩ = 1 S-RDCP(I_2Br_2), (e) ⟨n⟩ = 1 S-RDCP(I_1Br_3), and (f) ⟨n⟩ = 1 S-RDCP(Br_4).

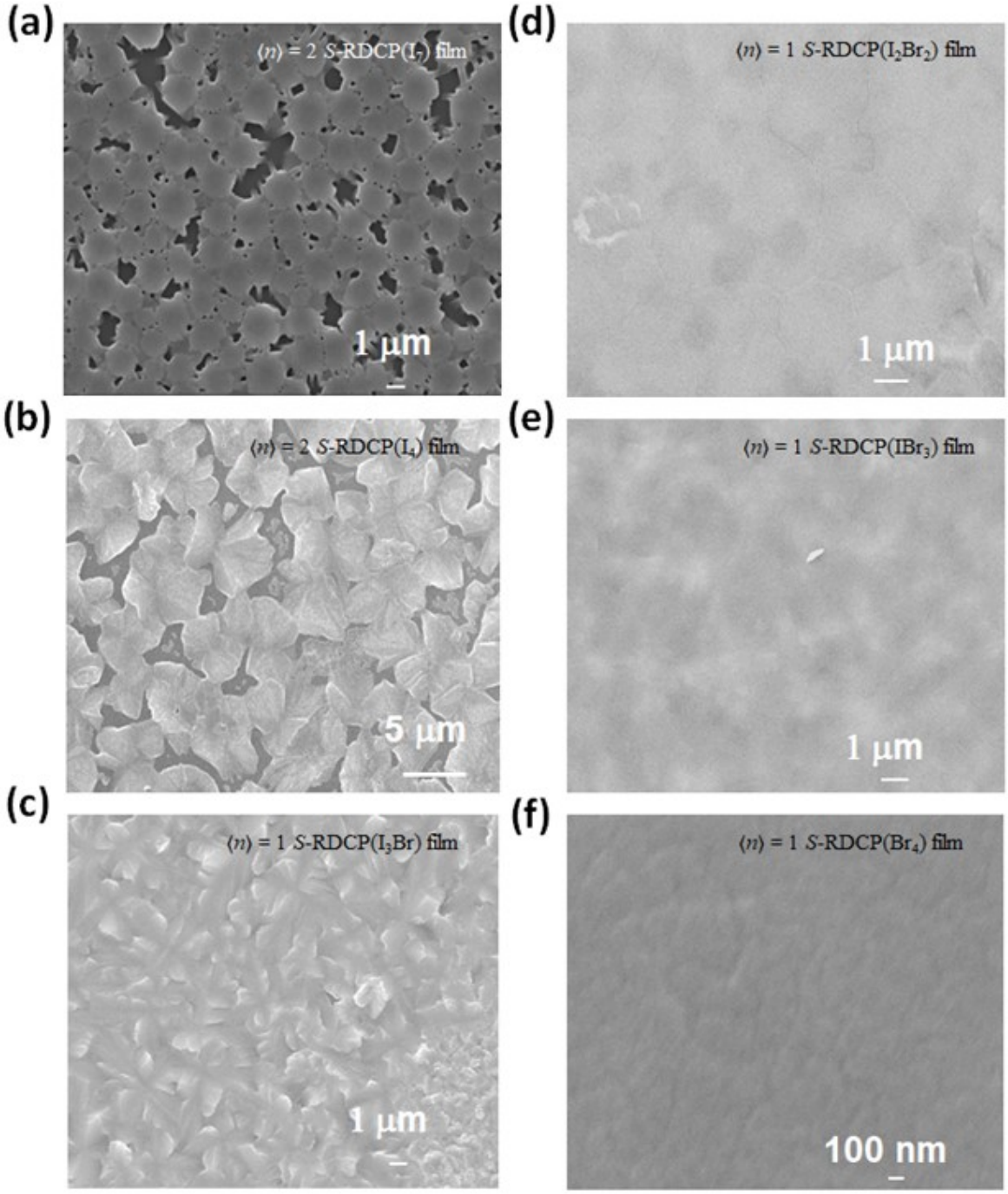

Figure S3 SEM images for (a) ⟨n⟩ = 2 S-RDCP(I_7) film, (b) ⟨n⟩ = 1 S-RDCP(I_4), (c) ⟨n⟩ = 1 S-RDCP(I_3Br), (d) ⟨n⟩ = 1 S-RDCP(I_2Br_2), (e) ⟨n⟩ = 1 S-RDCP(I_1Br_3), and (f) ⟨n⟩ = 1 S-RDCP(Br_4).

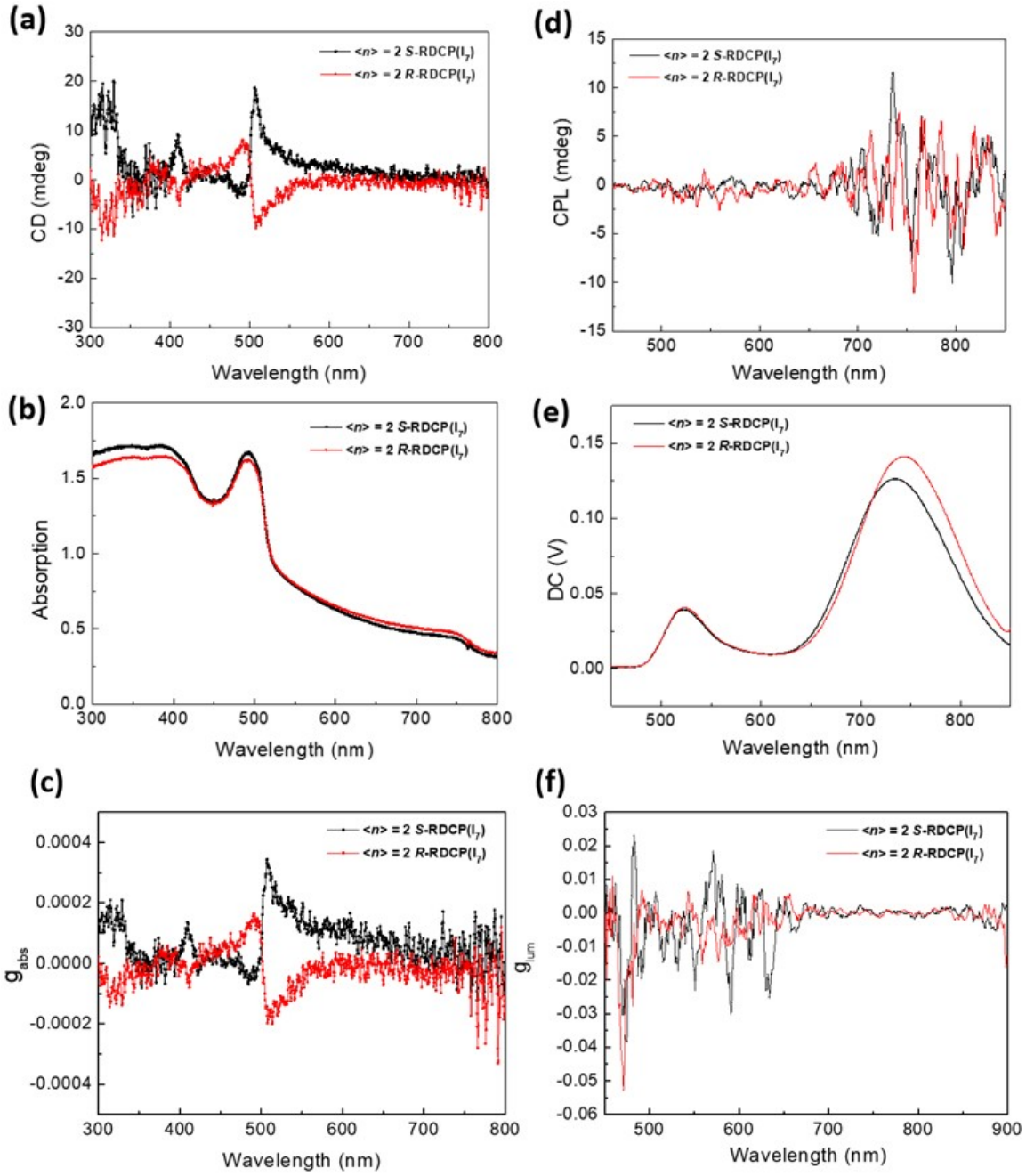

Figure S4 (a) CD spectra,(b) absorption, (c) g_{abs} value,(d) CPL spectra, (e) DC, and (f) g_{lum} value of R-/S-RDCP films with ⟨n⟩ = 2.

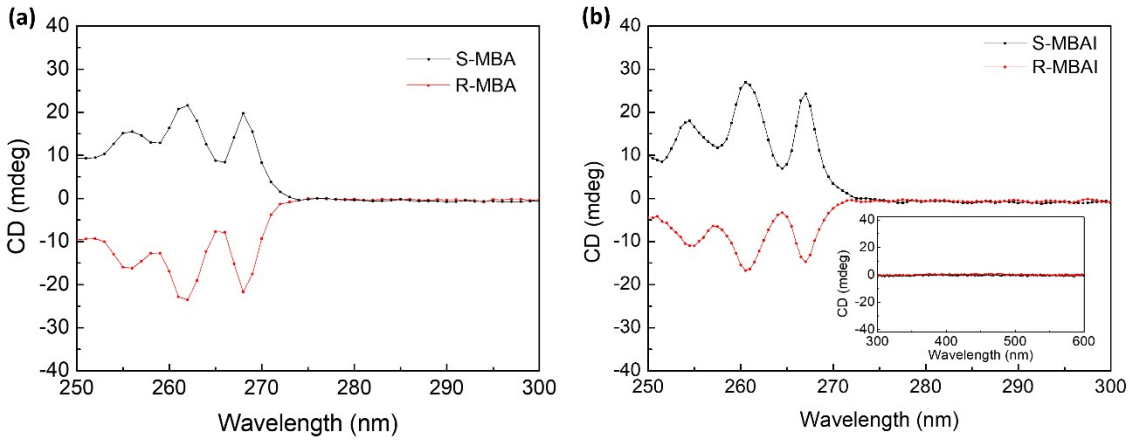

Figure S5 CD spectra of (a) *R*-/*S*-MBA and (b) *R*-/*S*-MBAI. The inset in (b) is the CD spectra of *R*-/*S*-MBAI at the wavelength ranges of 300 nm to 600 nm.

Supplementary Note 1: By means of the application of magnetic CD (MCD) spectrum, detailed information about the electronic states can be obtained.[1] The magneto-optically active and inactive electronic transitions can also be distinguished.[2] For ⟨n⟩ = 1 R-/S-RDCP film, apparent MCD signal can only be observed at the wavelength range of 450–550 nm (Figure S7). The gabs values (−0.003 ~ +0.003) were obtained. These derivative features change with increasing the strength and inversing the direction of the magnetic field. This phenomenon can be ascribed to the fact that the degenerate electronic structure of (R-/S-MBA)$_2$PbI$_4$ splits into multiple energy levels according to the condition of the external magnetic field (Zeeman splitting). No other MCD signal could be observed at the long wavelength range. However, for ⟨n⟩ = 2 R-/S-RDCP (I_7) film, in addition to the signals at the wavelength range of 450–550 nm, MCD signals at the wavelength range of 750–800 nm were also observed (Figure S8), indicating the presence of MAPbI3 in ⟨n⟩ = 2R-/S-RDCP(I7) film. The MCD signals of pure MAPbI$_3$ film without chiral ligand were presented in Figure S9(a)-(c). The degenerate energy level of MAPbI3 splits under a magnetic field and causes MCD signals around the absorption edge. The gabs values (−0.001 ~ +0.001) were obtained. The trend of MCD signals at the wavelength range of 450–550 nm is similar for both ⟨n⟩ = 1 and 2 R-/S-RDCP films, indicating that (R-/S-MBA)2PbI4 dominates the optical chirality properties at that wavelength range for both films.

(1) Pinchetti, V.; Di, Q.;Lorenzon, M.;Camellini, A.; Fasoli, M.;Zavelani-Rossi, M.;Meinardi, F.; Zhang, J.; Crooker, S. A.;Brovelli, S. Excitonic Pathway to Photoinduced Magnetism in Colloidal Nanocrystals with Nonmagnetic Dopants. *Nature Nanotechnology* **2018**, *13*, 145.

(2) Yang, J.;Fainblat, R.; Kwon, S. G.;Muckel, F.; Yu, J. H.;Terlinden, H.; Kim, B. H.;Iavarone, D.; Choi, M. K.; Kim, I. Y.; Park, I.; Hong, H. K.; Lee, J.; Son, J. S.; Lee, Z.; Kang, K.; Hwang, S. J.;Bacher, G.; Hyeon, T. Route to the Smallest Doped Semiconductor: Mn^{2+}-Doped $(CdSe)_{13}$ Clusters. *J. Am. Chem. Soc.***2015**, *137*, 12776.

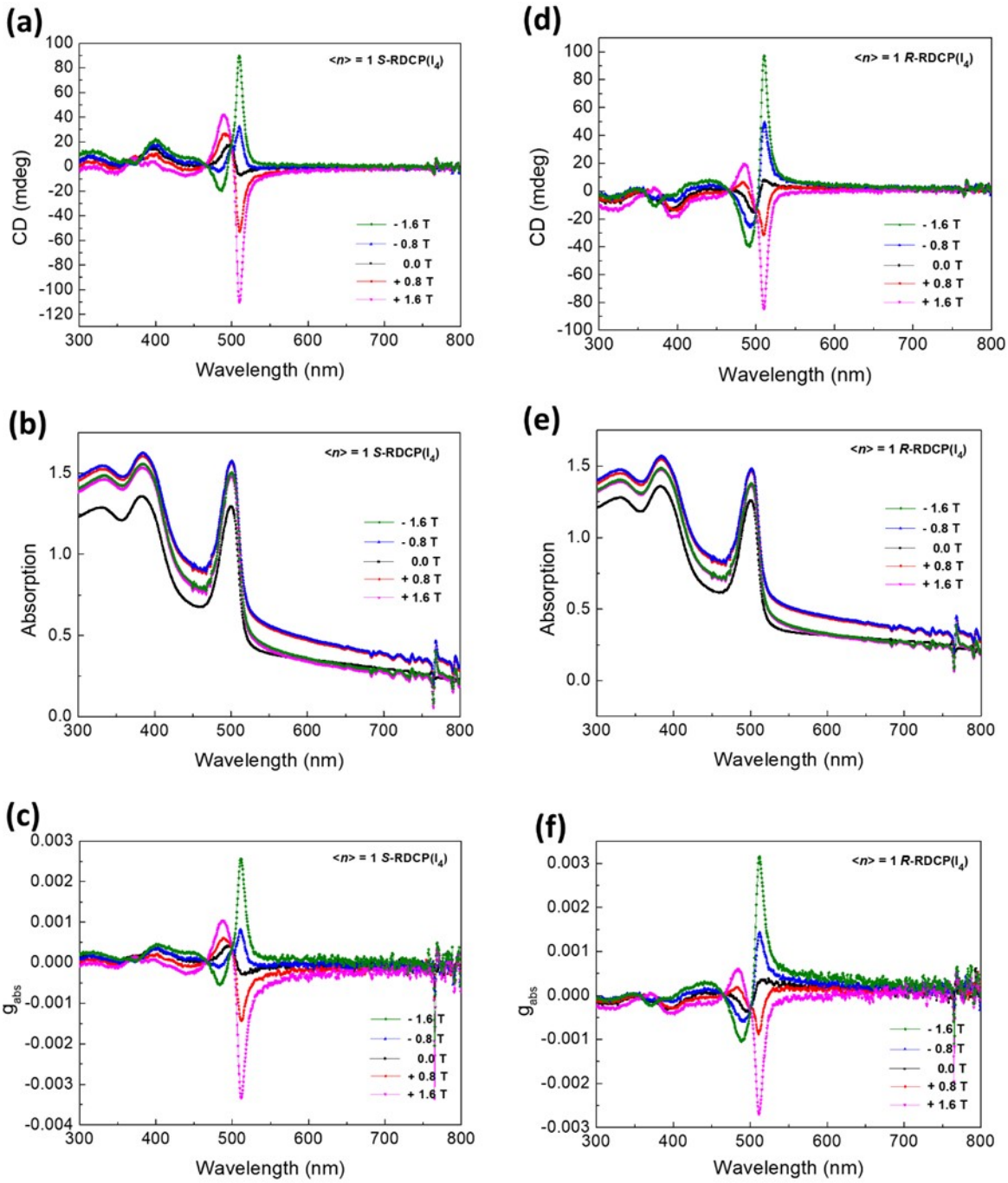

Figure S6(a),(d) CD, (b),(e) absorption, and (c),(f) g_{abs} spectra of⟨n⟩ = 1 (a),(b),(c) *S*-RDCP filmsand (d),(e),(f) *R*-RDCP films under different magnetic fields.

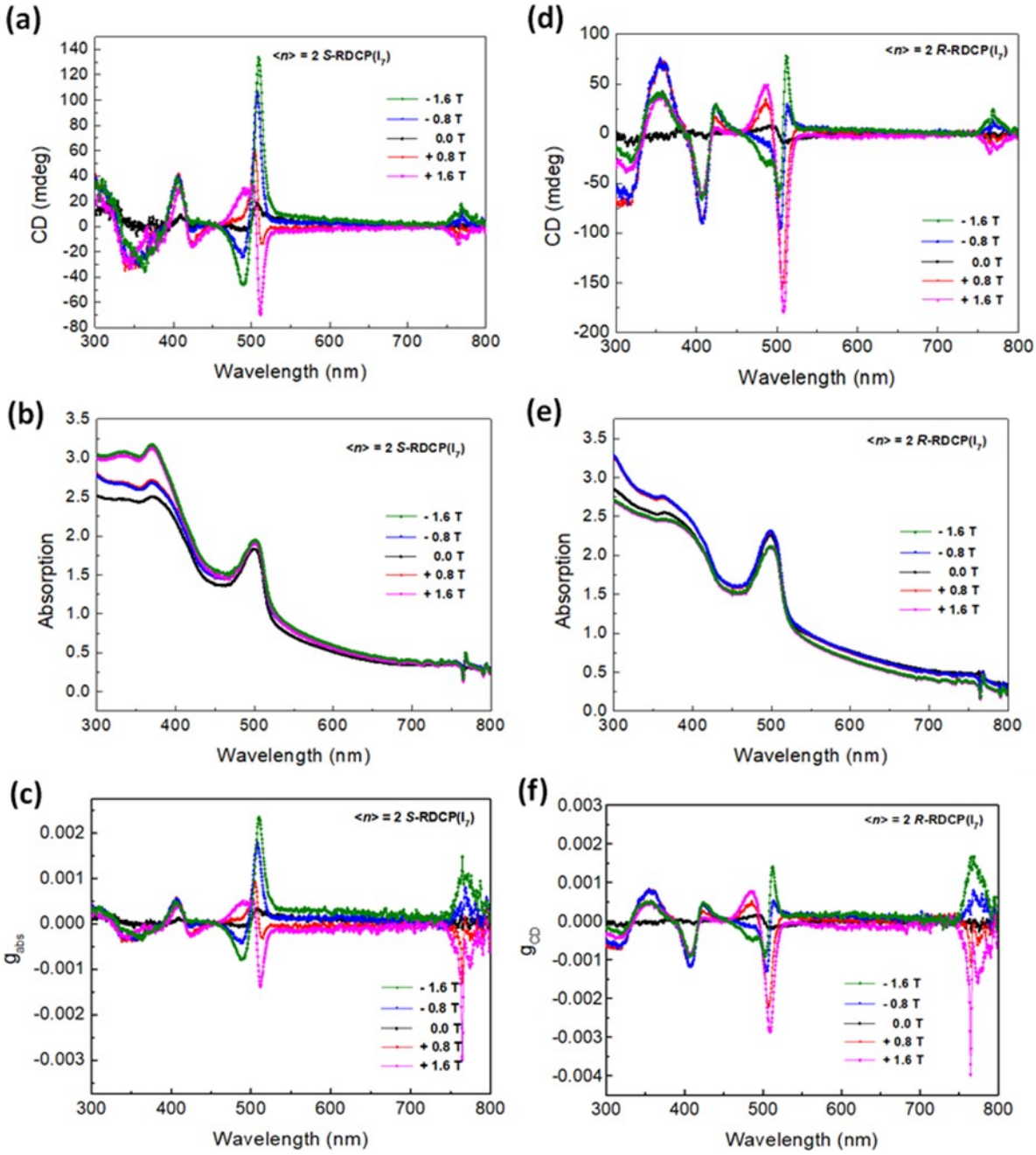

Figure S7 (a),(d) CD, (b),(e) absorption, and (c),(f) g_{abs} spectra of $\langle n \rangle = 2$ (a),(b),(c) *S*-RDCP films and (d),(e),(f) *R*-RDCP films under different magnetic fields.

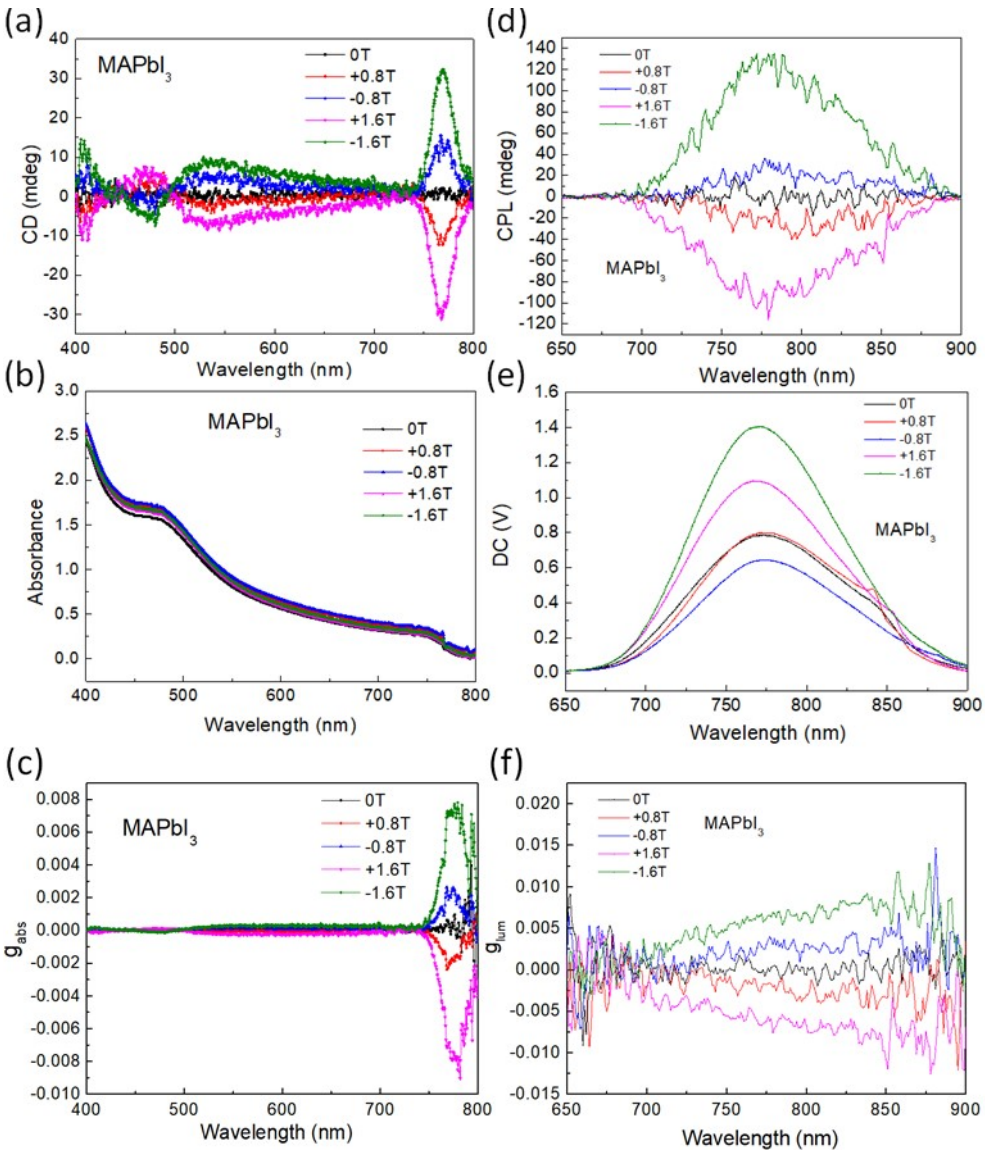

Figure S8 (a) CD, (b) absorption, and (c) g_{abs} spectra of pure $MAPbI_3$ films under various magnetic fields, and (d) CPL, (e) DC, and (f) g_{lum} spectra of pure $MAPbI_3$ films under different magnetic fields.

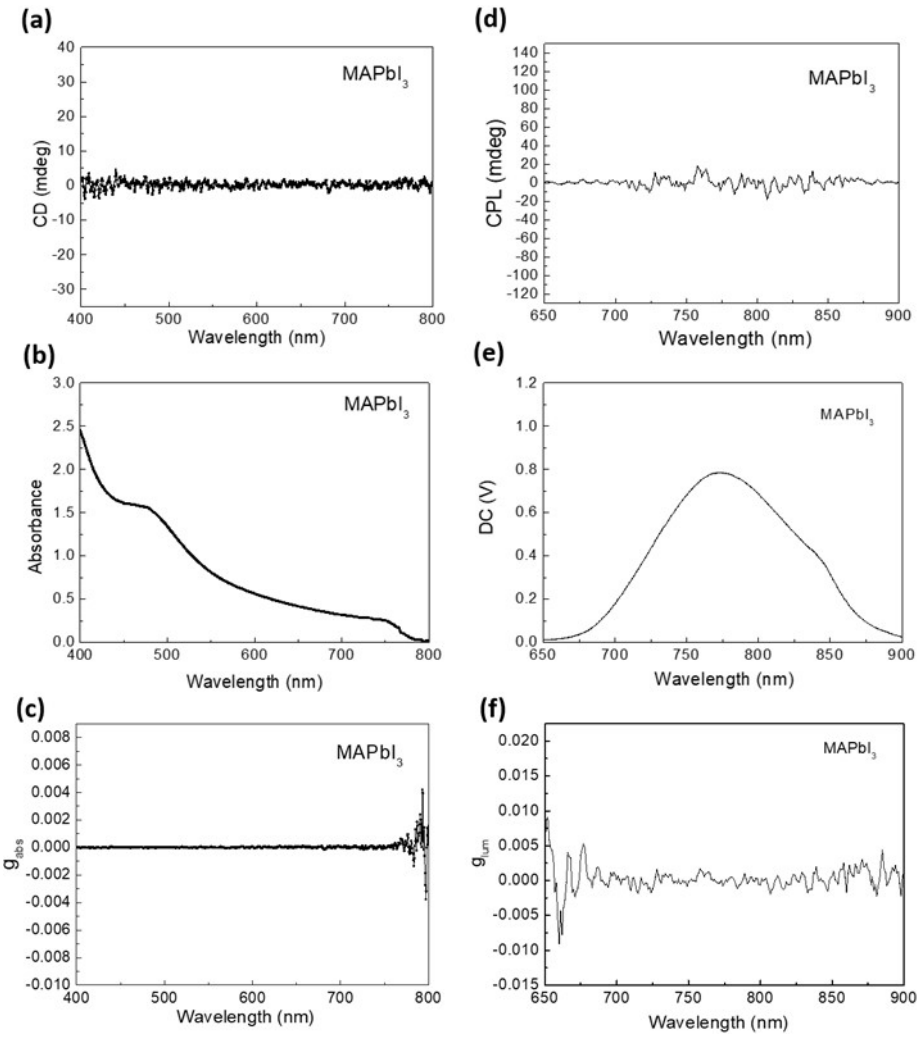

Figure S9 (a) CD spectra,(b) absorption, (c) g_{abs} value,(d) CPL spectra, (e) DC, and (f) g_{lum} value of $MAPbI_3$ 3D perovskite films.

Supplementary Note 2: For $\langle n \rangle$ = 1 *R*-/*S*-RDCP (I_4) film, the MCPL spectra showed similar curves under various magnetic fields (**Figure S10(a)** and **S10(d)**), indicating that the magnetic field had only a slight influence on MCPL. Corresponding g_{lum} values ~0.01 were observed (**Figure S10(c)** and **S10(f)**). As for $\langle n \rangle$ = 2 *R*-/*S*-RDCP (I_7) film, two mirror-like MCPL peaks were observed at the wavelength ranges of 470–650 nm and 650–900 nm (**Figure S11(a)** and **S11(d)**). The corresponding g_{lum} values less than ~0.005 were observed (**Figure S11(c)** and **S11(f)**).

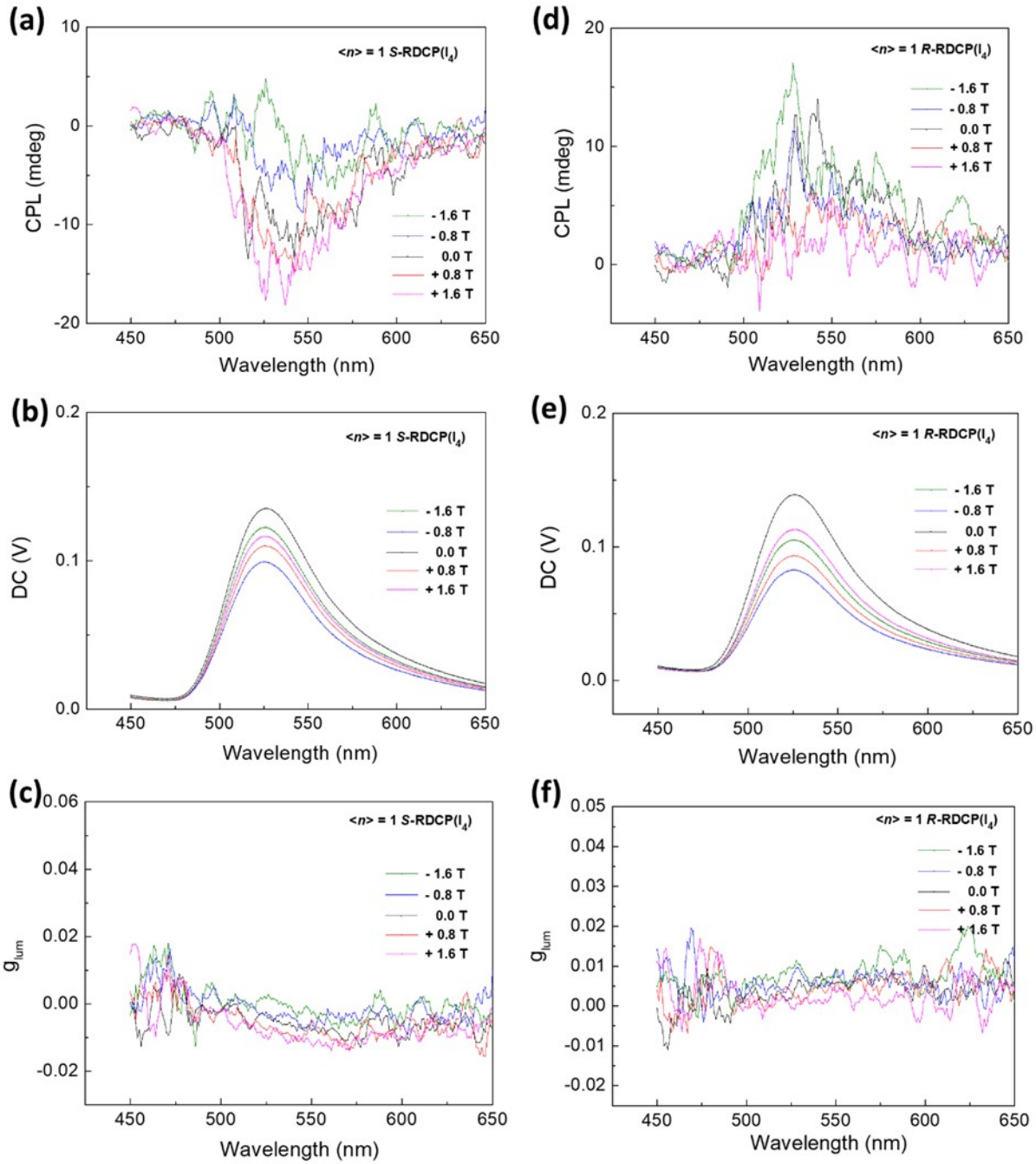

Figure S10 (a),(d) CPL, (b),(e) DC, and (c),(f) g_{lum} spectra of $\langle n \rangle = 1$ (a),(b),(c) *S*-RDCP films and (d),(e),(f) *R*-RDCP films under different magnetic fields.

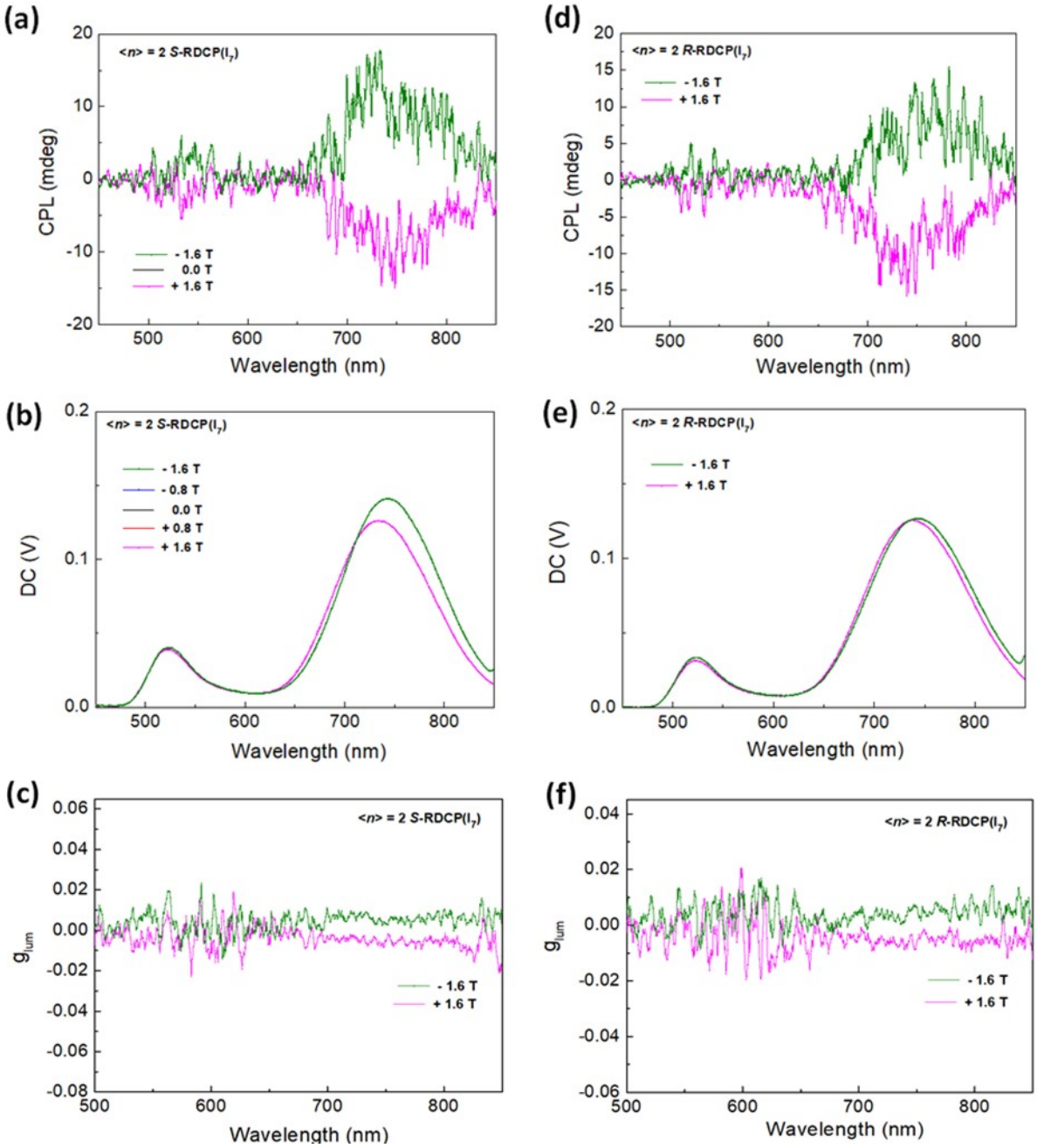

Figure S11 (a),(d) CPL, (b),(e) DC, and (c),(f) g_{lum} spectra of $\langle n \rangle = 2$ (a),(b),(c) *S*-RDCP films and (d),(e),(f) *R*-RDCP films under different magnetic fields.

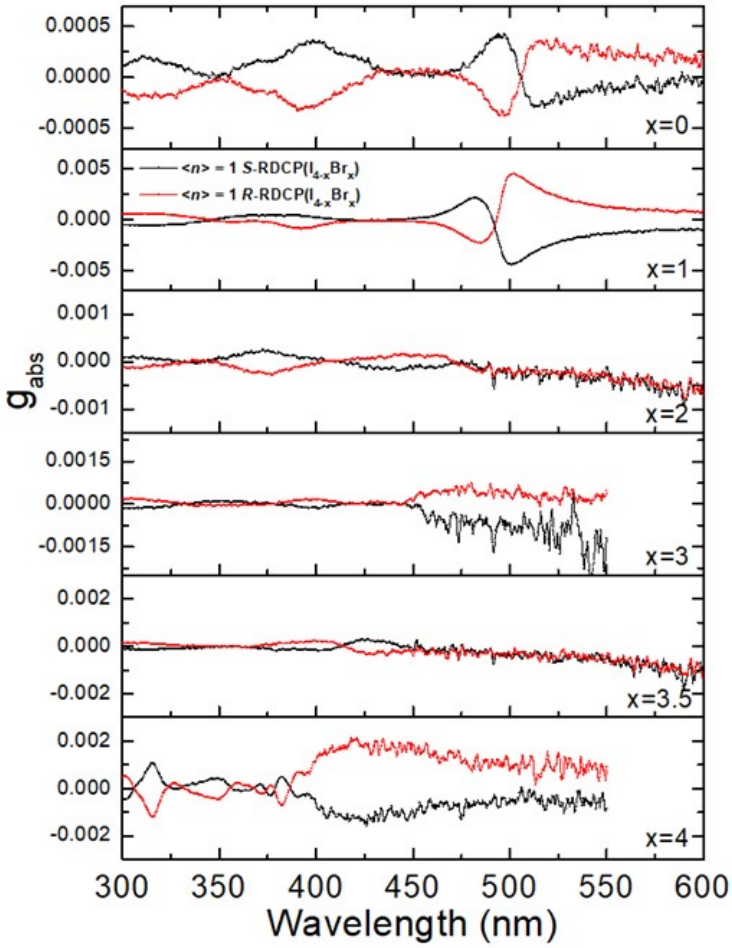

Figure S12 The g_{abs} spectra of $\langle n \rangle = 1$ *R*-/*S*-RDCP films with different halide compositions.

Supplementary Note 3: No other MCD signal could be observed at the long wavelength range. This phenomenon can be ascribed to the Zeeman splitting of the degenerate chiral absorbing states of (R-/S-MBA)$_2$Pb($I_{4-x}Br_x$). The gabs values in the range of −0.008 ~ +0.008 were observed around their exciton absorption peaks. The Zeeman splitting values of ⟨n⟩ = 1 R-/S-RDCP (I_4) were obtained via

$$\Delta E_Z = -\frac{\sqrt{2e}}{2}\sigma\frac{\Delta A_{peak} - \Delta A_{valley}}{A_0} \quad (1)$$

Where 2σ is Gaussian's full width at 1/e of the maximum absorption A_0 and where ΔA is the MCD intensity. The extracted ΔE_Zvalues are shown in **Table S1**. Without the application of magnetic field, the absolute values ofΔE_Z are a few ten μeV but with different signs, indicating the different chiralities of *R*-/*S*-RDCP films. Under magnetic fields, ΔE_Z varies from ~ −350 μeV to ~ 350 μeV with changing magnetic field from 1.6 T to – 1.6 T. The observed reversal signs of ΔE_Z under the opposite direction of the magnetic field indicates that the corresponding energy level splitting could be switched by the direction of the magnetic field. The obtained ΔE_Z values are in the same order of magnitude as previously reported values on RP phase 2D halide perovskites under a low magnetic field.[3-9]

(3) Dyksik, M.; Wang, S.;Paritmongkol, W.; Maude, D. K.; Tisdale, W. A.; Baranowski, M.;Plochocka, P. Tuning the Excitonic Properties of the 2D $(PEA)_2(MA)_{n-1}Pb_nI_{3n+1}$ Perovskite Family via Quantum Confinement. *J. Phys. Chem. Lett.***2021**, *12*, 6, 1638.
(4) Dyksik, M.;Duim, H.; Zhu, X.; Yang, Z.; Gen, M.;Kohama, Y.;Adjokatse, S.; Maude, D. K.;Loi, M. A.; Egger, D. A.; Baranowski, M.;Plochocka, P. Broad Tunability of Carrier Effective Masses in Two-Dimensional Halide Perovskites. *ACS Energy Lett.* **2020**, *5*, 3609.
(5) Baranowski, M.;Zelewski, S. J.;Kepenekian, M.;Traoré, B.; Urban, J. M.;Surrente, A.;Galkowski, K.; Maude, D. K.;Kuc, A.; Booker, E. P.;Kudrawiec, R.;Stranks, S. D.;Plochocka, P. Phase-Transition-Induced Carrier Mass Enhancement in 2D Ruddlesden–Popper Perovskites. *ACS Energy Lett*. **2019**, *4*, 2386.
(6) Blancon, J. C.; Stier, A. V.; Tsai, H.;Nie, W.;Stoumpos, C. C.;Traoré, B.;Pedesseau, L.;Kepenekian, M.;Katsutani, F.; Noe, G. T.;Kono, J.;Tretiak, S.; Crooker, S. A.; Katan, C.;Kanatzidis, M. G.; Crochet, J. J.; Even, J.; Mohite, A. D. Scaling Law for Excitons in 2D Perovskite Quantum Wells. *Nature Comm*. **2018**, *9*, 2254.
(7) Kataoka, T.; Kondo, T.; Ito, R.; Sasaki, S.; Uchida, K.; Miura, N. Magneto-Optical Study on Excitonic Spectra in $(C_6H_{13}NH_3)_2PbI_4$. *Phys. Rev. B* **1993**, *47*, 2010.
(8) Hirasawa, M.; Ishihara, T.;Goto, T.; Sasaki, S.; Uchida, K.; Miura, N. Magnetoreflection of the Lowest Exciton in a Layered Perovskite-Type Compound $(C_{10}H_{21}NH_3)_2PbI_4$. *Solid State Communications* **1993**, *86*, 479.
(9) Xu, C.;Sakakura, H.; Kondo, T.; Takeyama, S.; Miura, N.; Takahashi, Y.;Kumata, K.; Ito, R. Magneto-Optical Effects of Excitons in $(C_{10}H_{21}NH_3)_2PbI_4$ under High Magnetic Fields up to 40 T. *Solid State Communications* **1991**, *79*, 249.

Table S1. $^{\Delta E_Z}$for MCD spectra of $\langle n \rangle$ = 1 *R*-/*S*-RDCP films.

B	-1.6 T	-0.8 T	0.0 T	0.8 T	1.6 T
S-RDCP	-0.000256	-0.000083	0.000028	0.000180	0.000360
R-RDCP	-0.000354	-0.000179	-0.000060	0.000091	0.000270

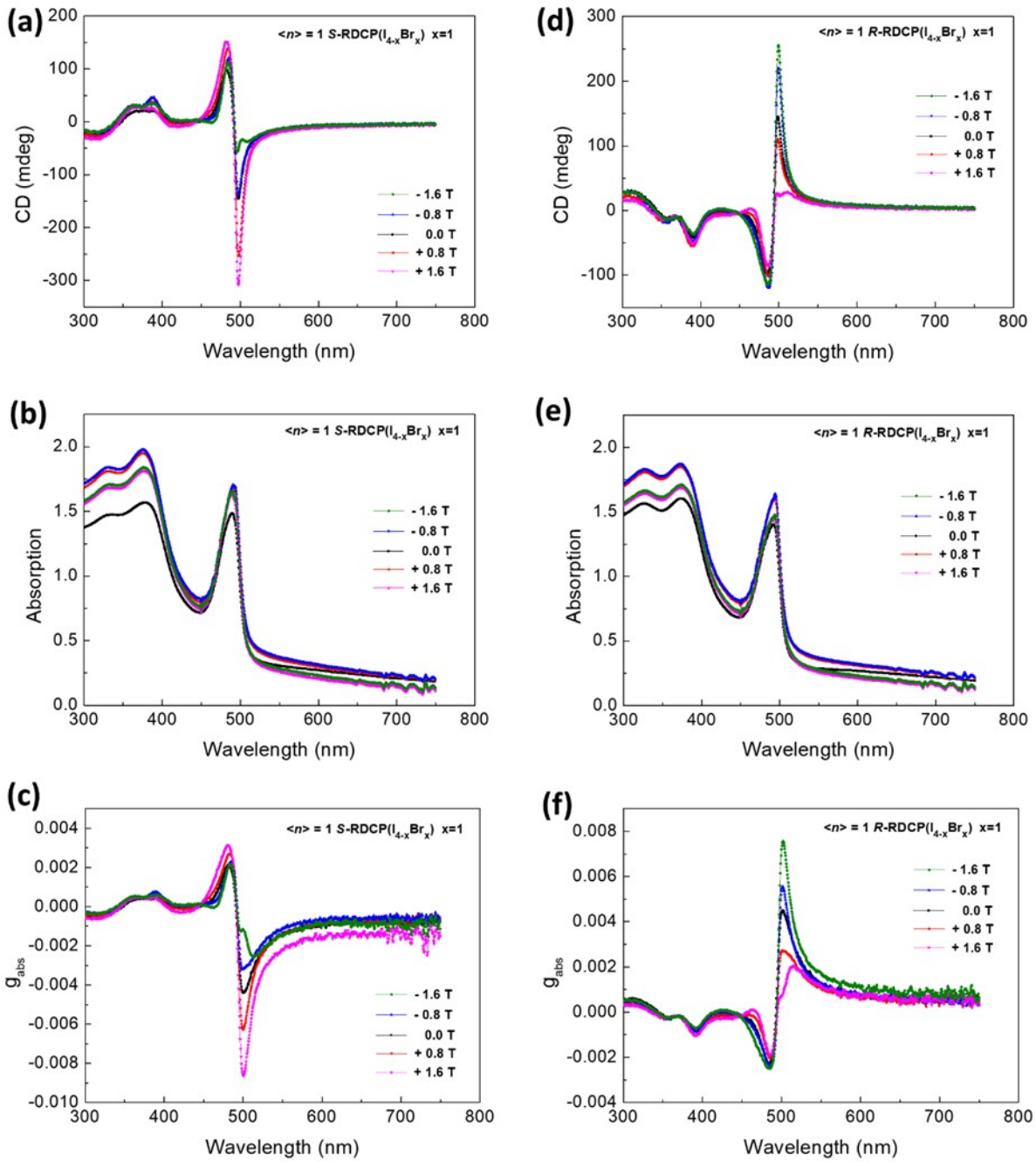

Figure S13 (a),(d) CD, (b),(e) absorption, and (c),(f) g_{abs} spectra of $\langle n \rangle = 1$ (a),(b),(c) *S*-RDCP($I_{4-x}Br_x$) ($x = 1$) films and (d),(e),(f) *R*-RDCP($I_{4-x}Br_x$) ($x = 1$) films under different magnetic fields.

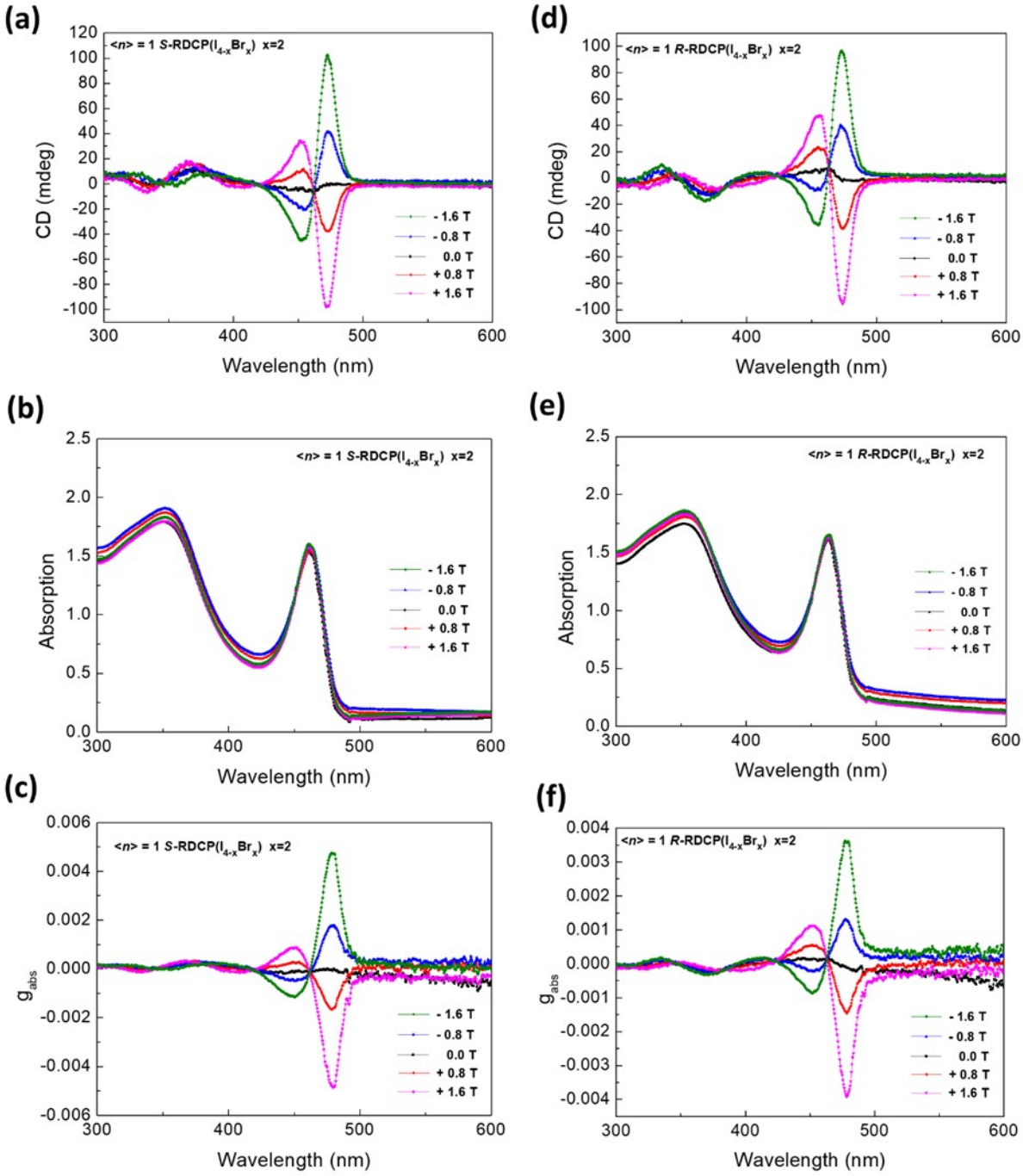

Figure S14 (a),(d) CD, (b),(e) absorption, and (c),(f) g_{abs} spectra of $\langle n \rangle = 1$ (a),(b),(c) *S*-RDCP($I_{4-x}Br_x$) ($x = 2$) films and (d),(e),(f) *R*-RDCP($I_{4-x}Br_x$) ($x = 2$) films under different magnetic fields.

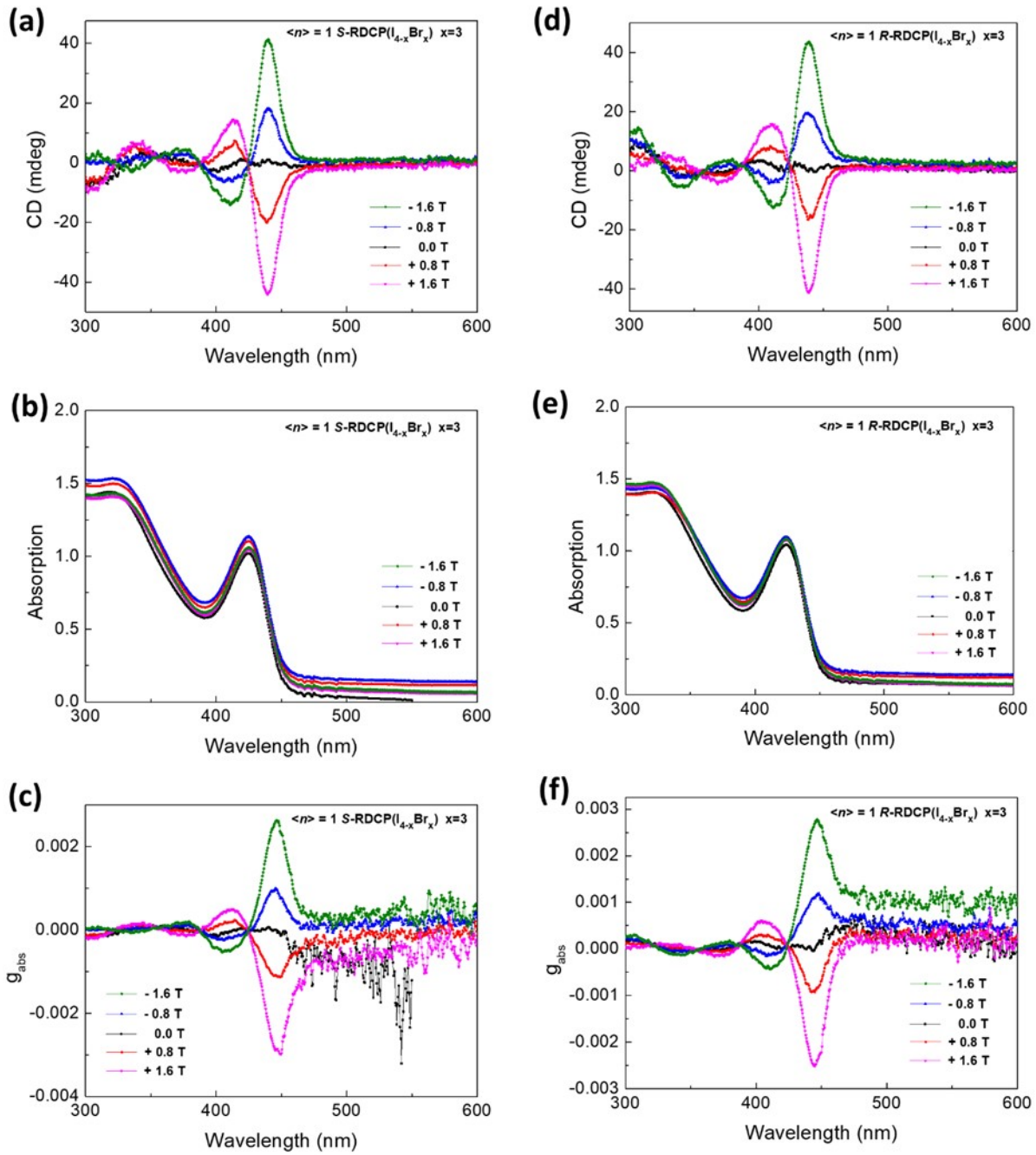

Figure S15 (a),(d) CD, (b),(e) absorption, and (c),(f) g_{abs} spectra of $\langle n \rangle = 1$ (a),(b),(c) *S*-RDCP($I_{4-x}Br_x$) ($x = 3$) films and (d),(e),(f) *R*-RDCP($I_{4-x}Br_x$) ($x = 3$) films under different magnetic fields.

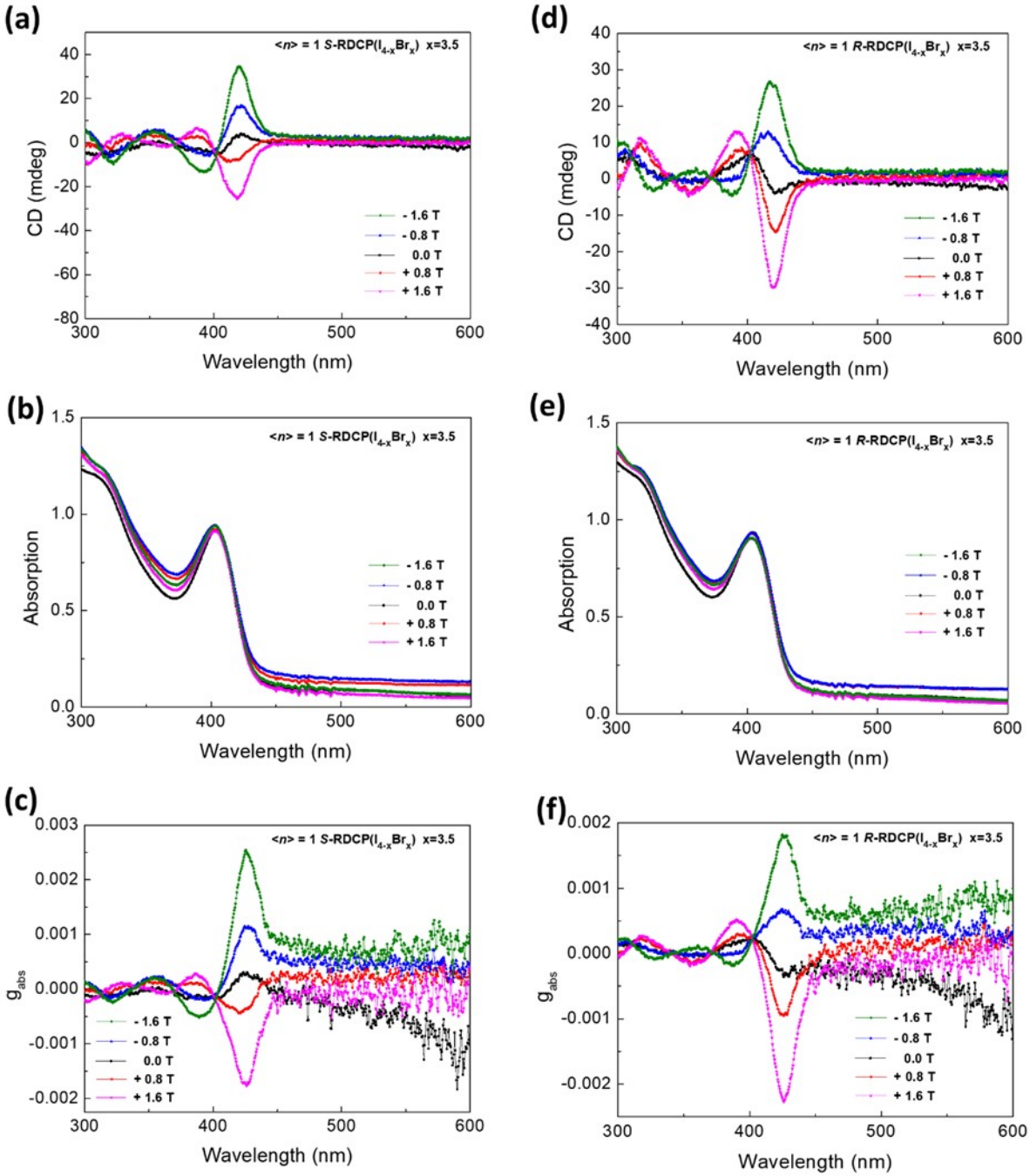

Figure S16 (a),(d) CD, (b),(e) absorption, and (c),(f) g_{abs} spectra of $\langle n \rangle = 1$ (a),(b),(c) *S*-RDCP($I_{4-x}Br_x$) ($x = 3.5$) films and (d),(e),(f) *R*-RDCP($I_{4-x}Br_x$) ($x = 3.5$) films under different magnetic fields.

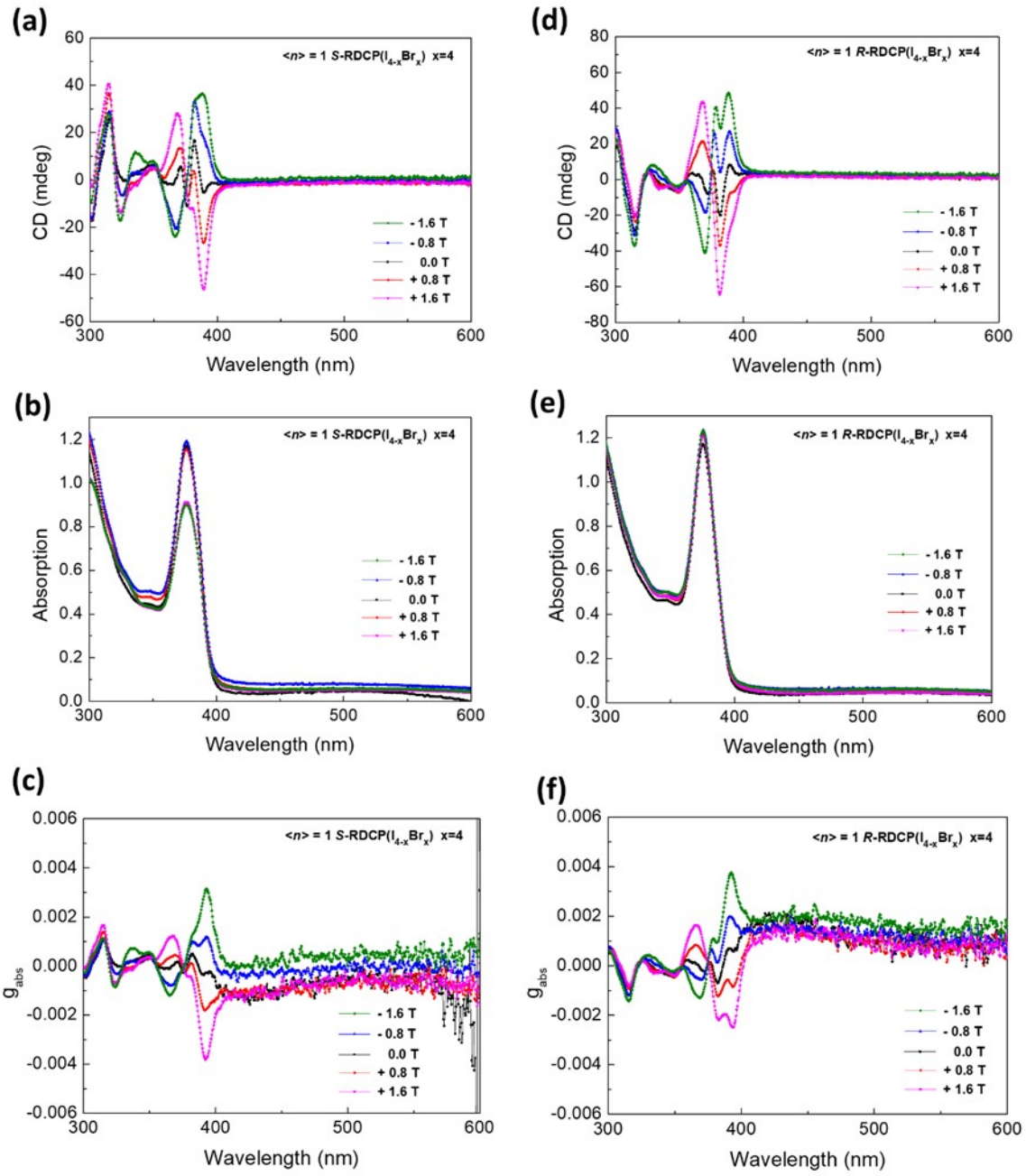

Figure S17 (a),(d) CD, (b),(e) absorption, and (c),(f) g_{abs} spectra of $\langle n \rangle = 1$ (a),(b),(c) *S*-RDCP($I_{4-x}Br_x$) ($x = 4$) films and (d),(e),(f) *R*-RDCP($I_{4-x}Br_x$) ($x = 4$) films under different magnetic fields.

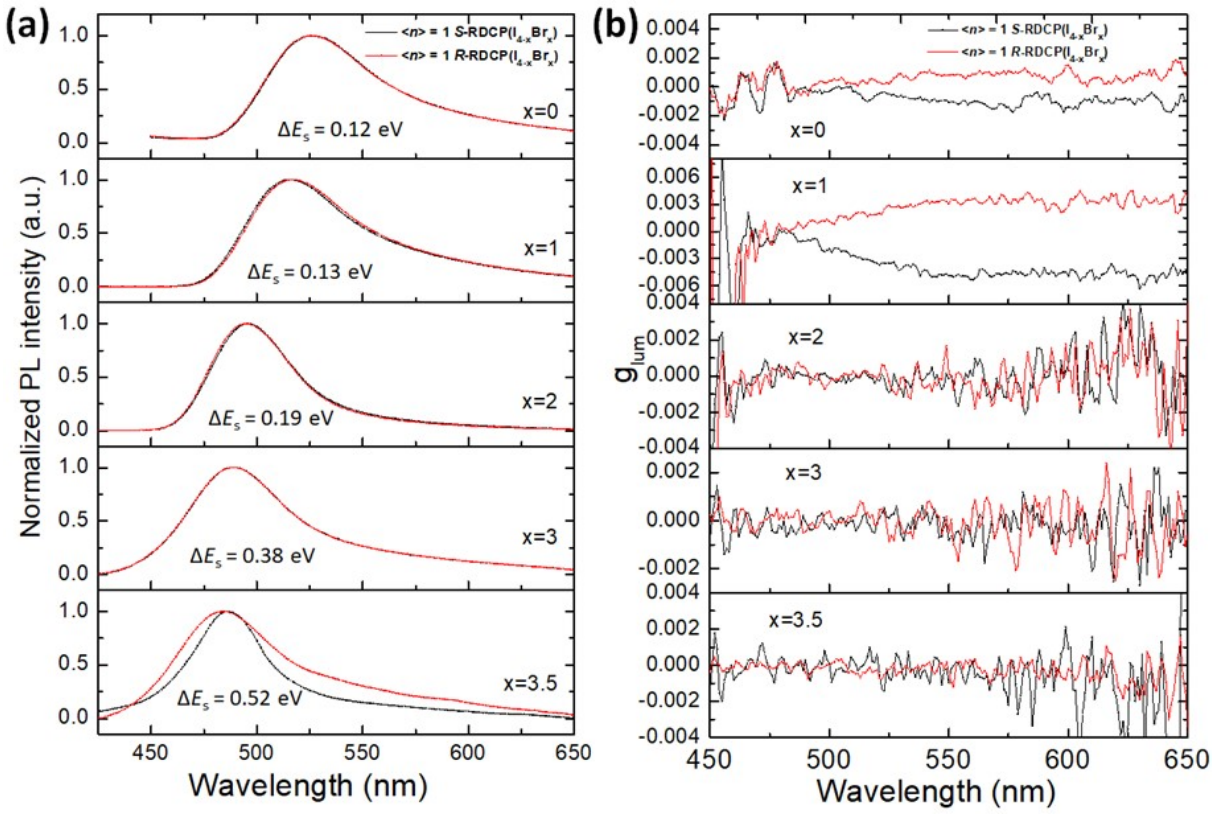

Figure S18 (a) The PL spectra and (b) g_{lum} of $\langle n \rangle = 1$ *R*-/*S*-RDCP films with different halide compositions.

Supplementary Note 4: For the MCPL spectra of $\langle n \rangle = 1$ *R*-/*S*-RDCP ($I_{4-x}Br_x$) ($x = 0$ and 1) films, the MCPL spectra resemble the one without applying magnetic field, and the magnetic field has only a slight or negligible influence on MCPL spectra. The g_{abs} value is approximately +0.005 ~ +0.01 for $\langle n \rangle = 1$ *R*-RDCP(I_4), −0.005 ~ −0.01 for $\langle n \rangle = 1$ *S*-RDCP(I_4), +0.015 ~ +0.02 for $\langle n \rangle = 1$ *R*-RDCP (I_3Br) and −0.01 ~ −0.02 for $\langle n \rangle = 1$ *S*-RDCP (I_3Br). However, the application of a magnetic field induced apparent mirror-image symmetric MCPL spectra when $x \geq 2$. These results indicated that the achiral deep self-trapped exciton state of $\langle n \rangle = 1$ *R*-/*S*-RDCP ($I_{4-x}Br_x$) ($x \geq 2$) is degenerate, while the chiral emissive state of $\langle n \rangle = 1$ *R*-/*S*-RDCP ($I_{4-x}Br_x$) ($x = 0$ and 1) tends to be non-degenerate.

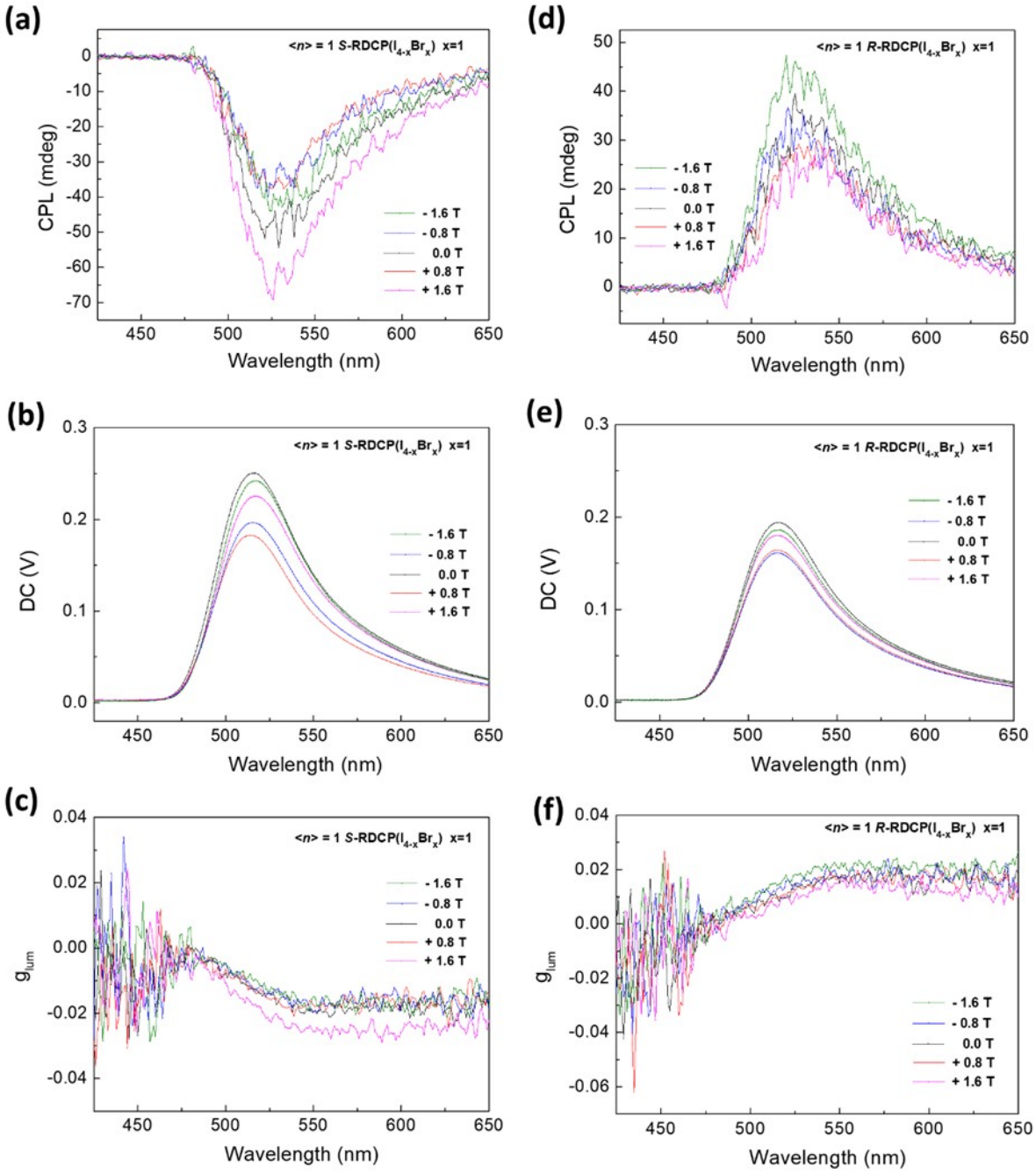

Figure S19 (a),(d) CPL, (b),(e) DC, and (c),(f) g_{lum} spectra of $\langle n \rangle = 1$ (a),(b),(c) *S*-RDCP($I_{4-x}Br_x$) ($x = 1$) films and (d),(e),(f) *R*-RDCP($I_{4-x}Br_x$) ($x = 1$) films under different magnetic fields.

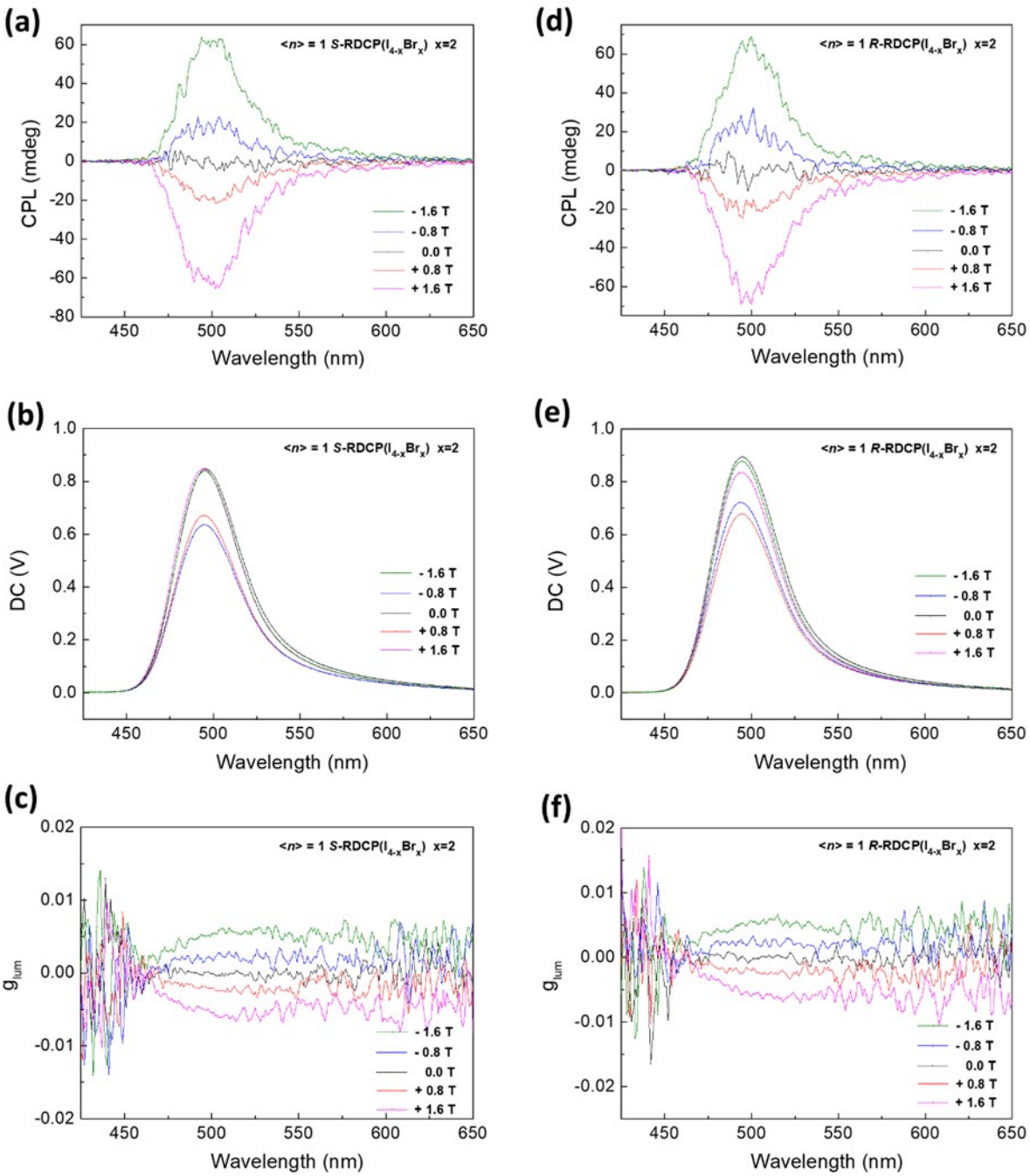

Figure S20 (a),(d) CPL, (b),(e) DC, and (c),(f) g_{lum} spectra of $\langle n \rangle = 1$ (a),(b),(c) *S*-RDCP($I_{4-x}Br_x$) ($x = 2$) films and (d),(e),(f) *R*-RDCP($I_{4-x}Br_x$) ($x = 2$) films under different magnetic fields.

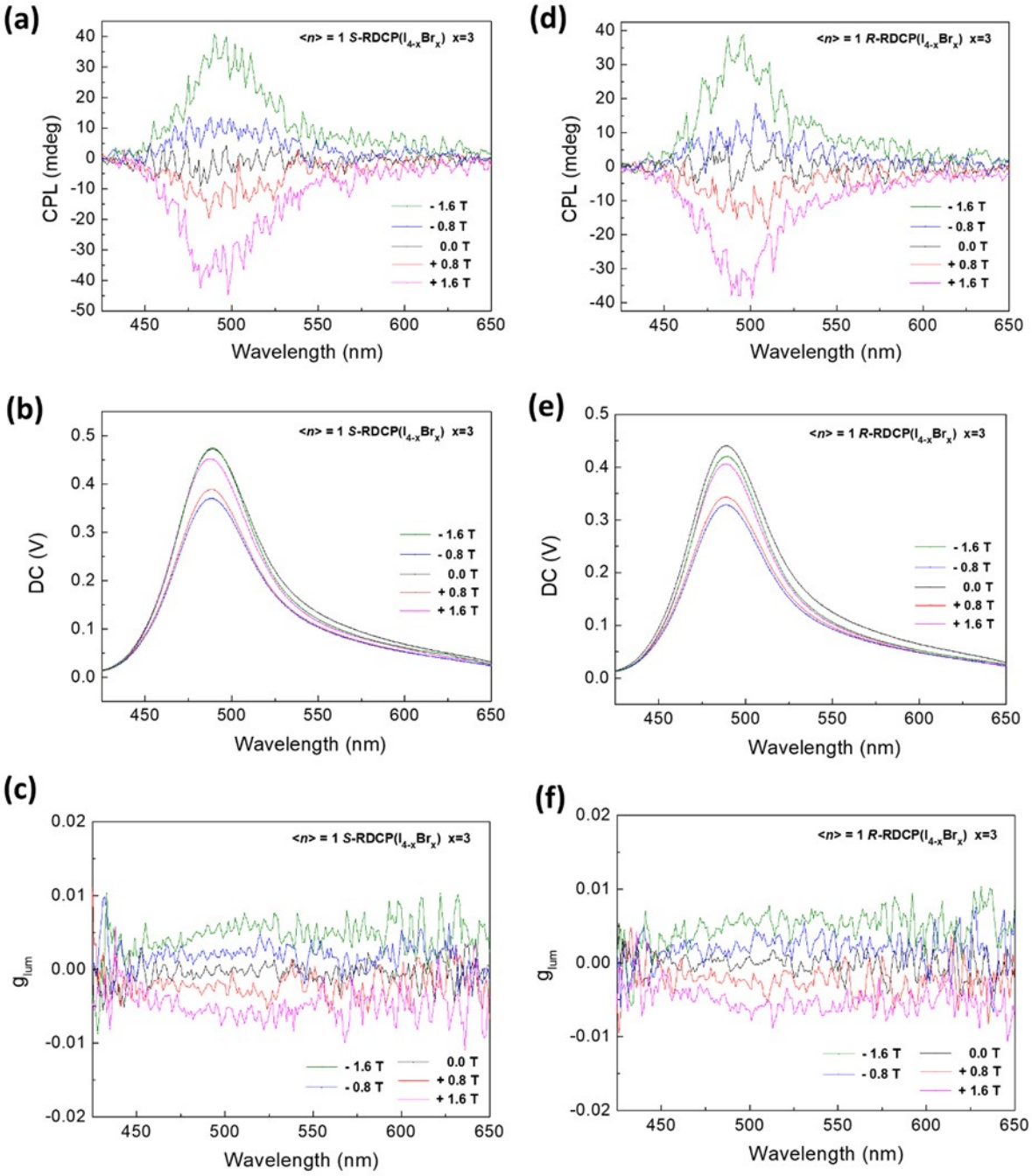

Figure S21 (a),(d) CPL, (b),(e) DC, and (c),(f) g_{lum} spectra of $\langle n \rangle = 1$ (a),(b),(c) *S*-RDCP($I_{4-x}Br_x$) ($x = 3$) films and (d),(e),(f) *R*-RDCP($I_{4-x}Br_x$) ($x = 3$) films under different magnetic fields.

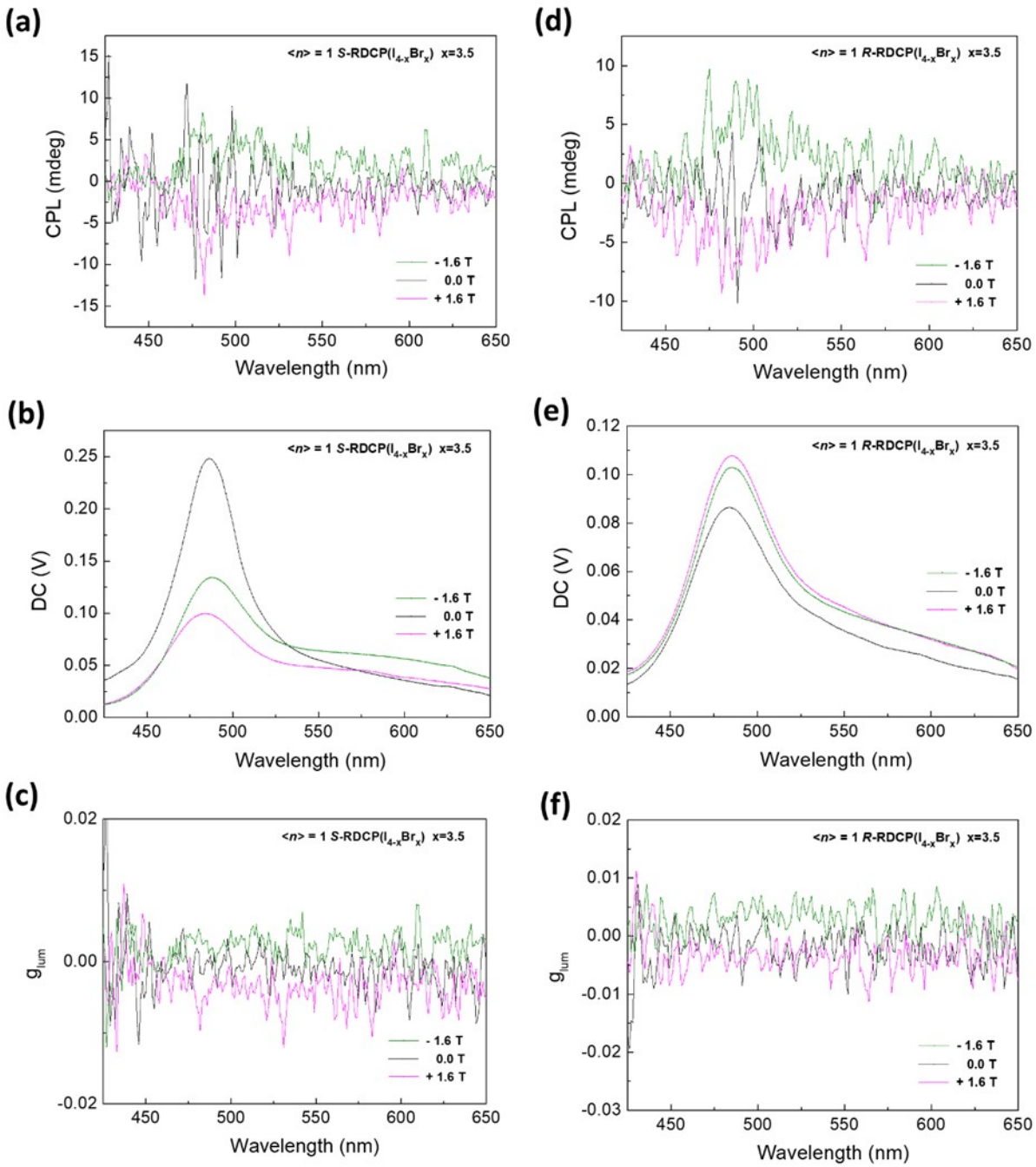

Figure S22 (a),(d) CPL, (b),(e) DC, and (c),(f) g_{lum} spectra of $\langle n \rangle = 1$ (a),(b),(c) *S*-RDCP($I_{4-x}Br_x$) ($x = 3.5$) films and (d),(e),(f) *R*-RDCP($I_{4-x}Br_x$) ($x = 3.5$) films under different magnetic fields.

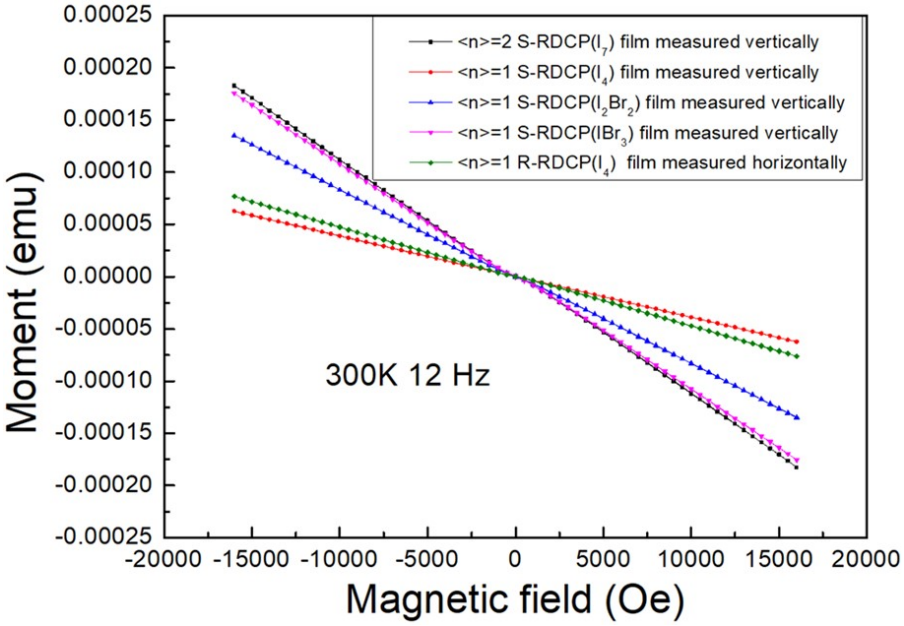

Figure S23 The M-H hysteresis curves of the chiral perovskite with different halide compositions

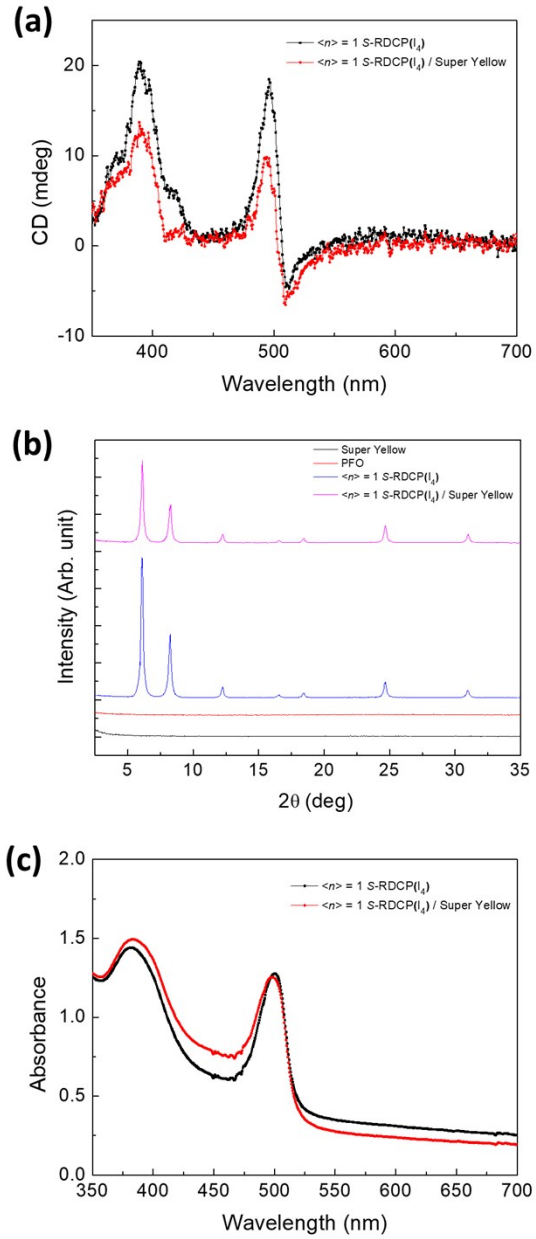

Figure S24 (a) CD spectra, (b) XRD patterns, and (c) absorption spectra of different films.

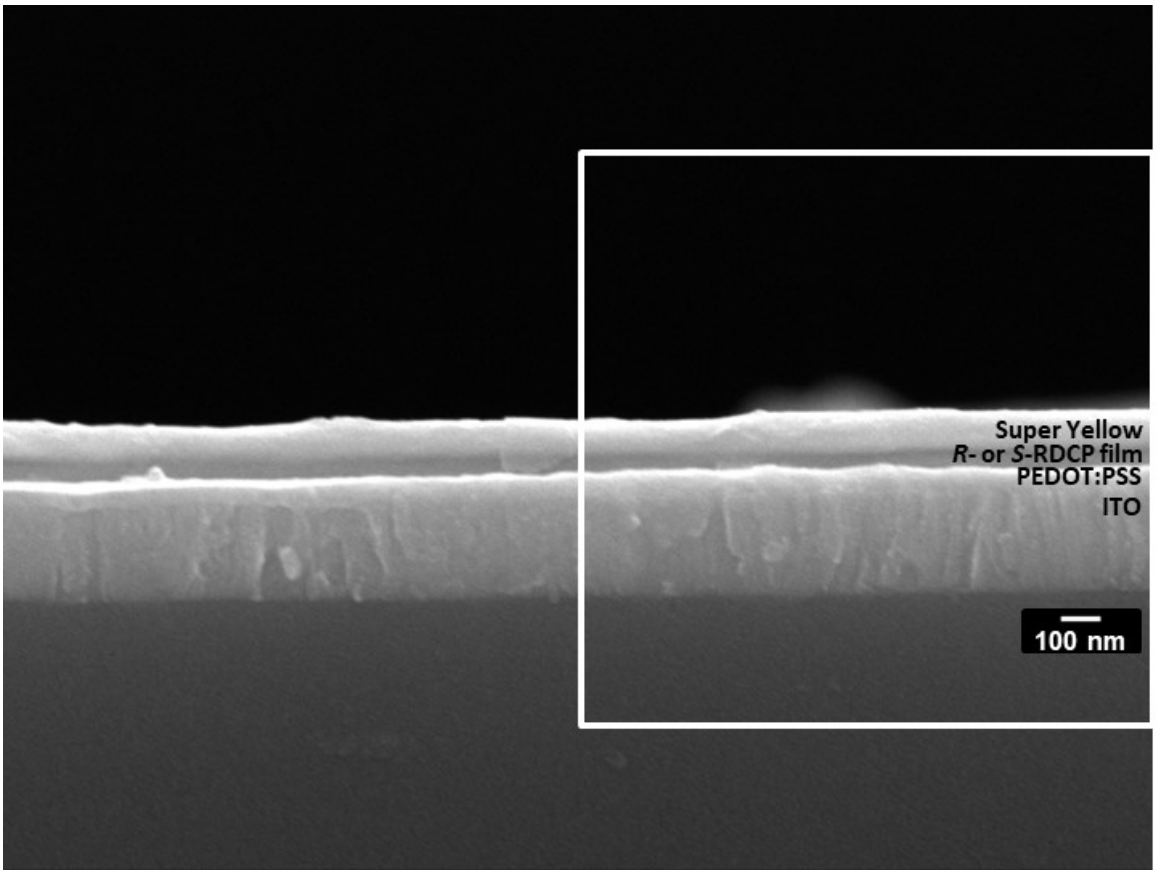

Figure S25 Cross-sectional SEM image of the spin-OLED device with chiral perovskite as the spin filter. The TPBi and the electrode were not deposited.

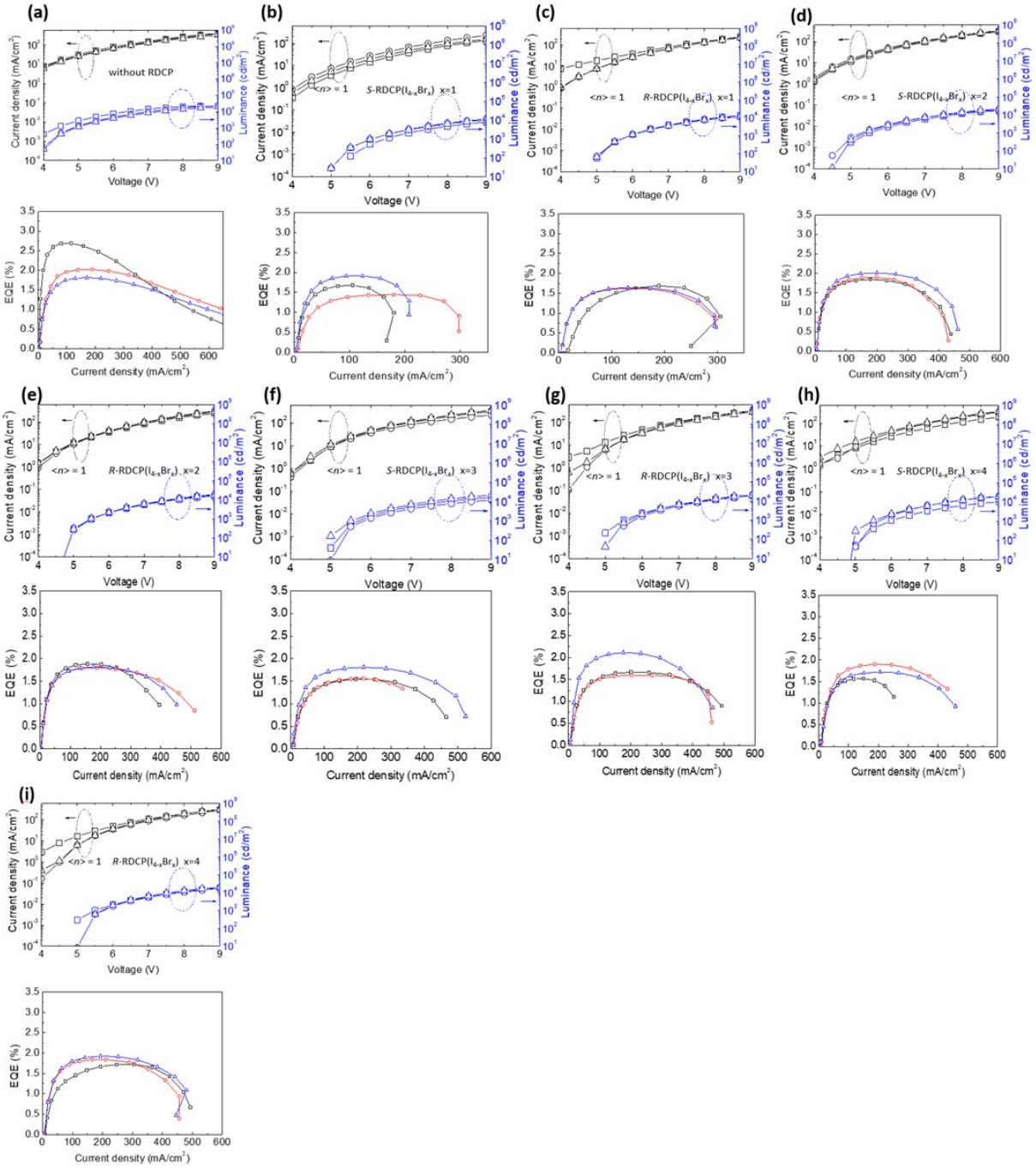

Figure S26 The J-V-L curves and EQE-J of the spin-OLEDs (a) without RDCP film,(b) with ⟨*n*⟩ = 1 *S*-RDCP($I_{4-x}Br_x$) (x = 1), (c) with ⟨*n*⟩ = 1 *R*-RDCP($I_{4-x}Br_x$) (x = 1), (d) with ⟨*n*⟩ = 1 *S*-RDCP($I_{4-x}Br_x$) (x = 2), (e) with ⟨*n*⟩ = 1 *R*-RDCP($I_{4-x}Br_x$) (x = 2), (f) with ⟨*n*⟩ = 1 *S*-RDCP($I_{4-x}Br_x$) (x = 3), (g) with ⟨*n*⟩ = 1 *R*-RDCP($I_{4-x}Br_x$) (x = 3), (h) with ⟨*n*⟩ = 1 *S*-RDCP($I_{4-x}Br_x$) (x = 4), (i) with ⟨*n*⟩ = 1 *R*-RDCP($I_{4-x}Br_x$) (x = 4).

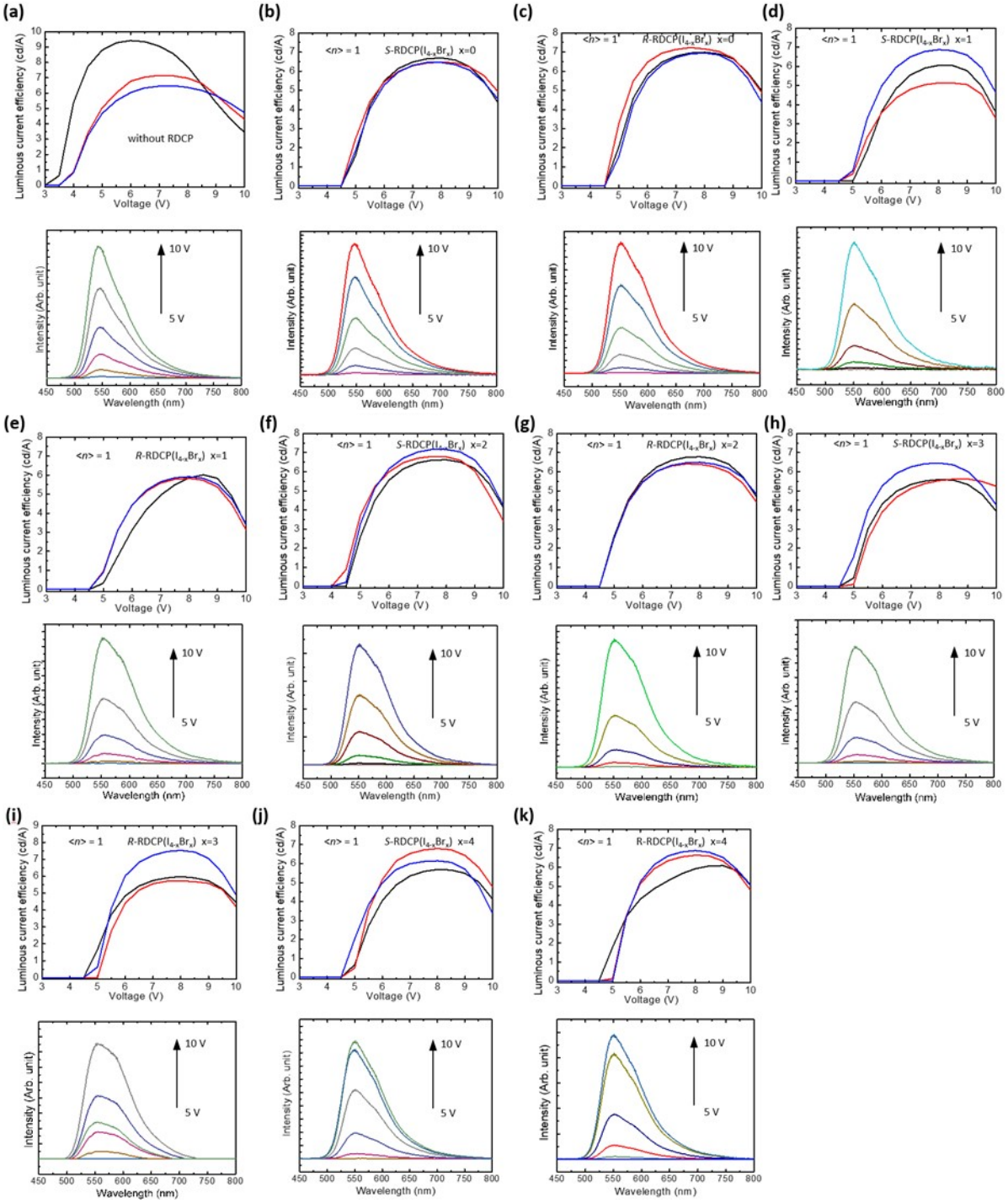

Figure S27 Current efficiency and EL spectra under different bias voltages of the spin-OLEDs (a) without RDCP film, (b) with ⟨*n*⟩ = 1 *S*-RDCP($I_{4-x}Br_x$) (x = 0), (c) with ⟨*n*⟩ = 1 *R*-RDCP($I_{4-x}Br_x$) (x = 0), (d) with ⟨*n*⟩ = 1 *S*-RDCP($I_{4-x}Br_x$) (x = 1), (e) with ⟨*n*⟩ = 1 *R*-RDCP($I_{4-x}Br_x$) (x = 1), (f) with ⟨*n*⟩ = 1 *S*-RDCP($I_{4-x}Br_x$) (x = 2), (g) with ⟨*n*⟩ = 1 *R*-RDCP($I_{4-x}Br_x$) (x = 2), (h) with ⟨*n*⟩ = 1 *S*-RDCP($I_{4-x}Br_x$) (x = 3), (i) with ⟨*n*⟩ = 1 *R*-RDCP($I_{4-x}Br_x$) (x = 3), (j) with ⟨*n*⟩ = 1 *S*-RDCP($I_{4-x}Br_x$) (x = 4), (k) with ⟨*n*⟩ = 1 *R*-RDCP($I_{4-x}Br_x$) (x = 4).

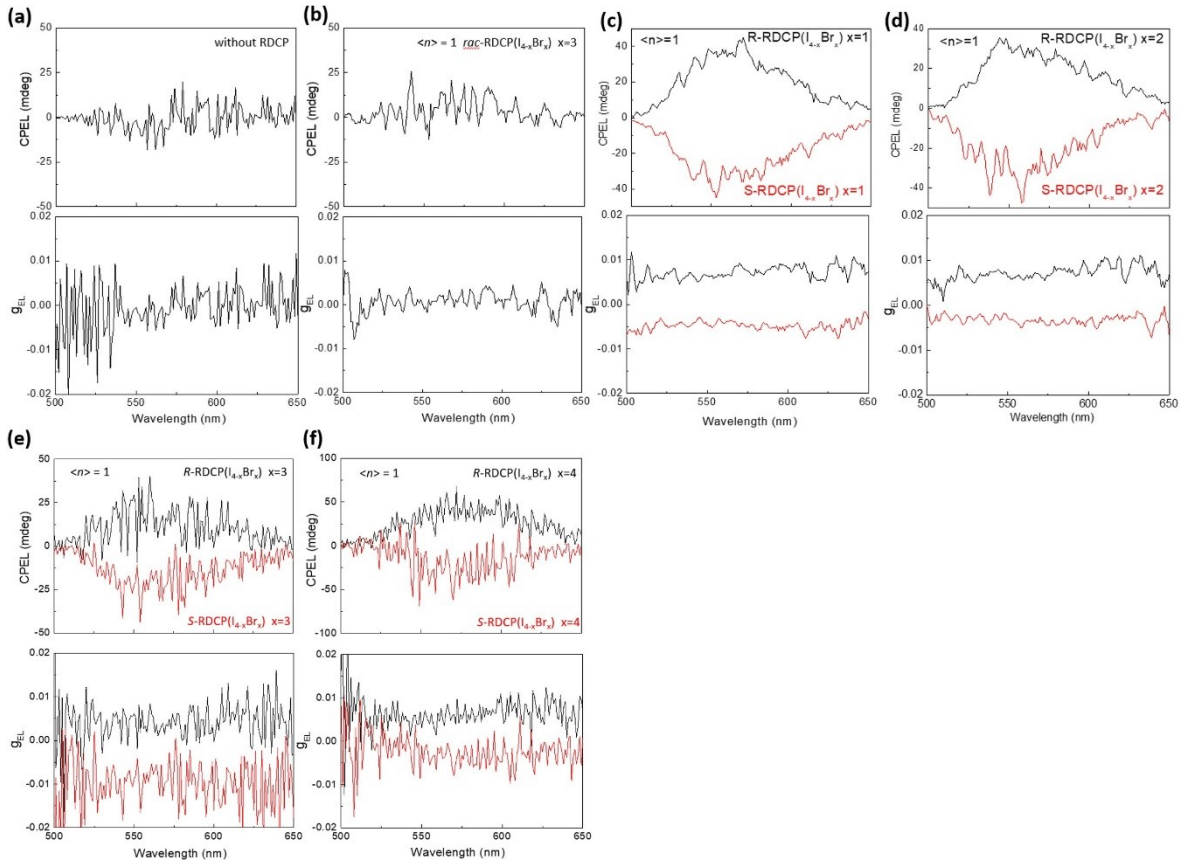

Figure S28 CPEL and g_{EL} spectra of the spin-OLED (a) without RDCP film, (b) with $\langle n \rangle = 1$ *rac*-RDCP($I_{4-x}Br_x$) (x = 3), (c) with $\langle n \rangle = 1$ *S*-/R-RDCP($I_{4-x}Br_x$) (x = 1), (d) with $\langle n \rangle = 1$ *S*-/ R-RDCP($I_{4-x}Br_x$) (x = 2), (e) with $\langle n \rangle = 1$ *S*-/ R-RDCP($I_{4-x}Br_x$) (x = 3), (f) with $\langle n \rangle = 1$ *S*-/ R-RDCP($I_{4-x}Br_x$) (x = 4) as spin filters.

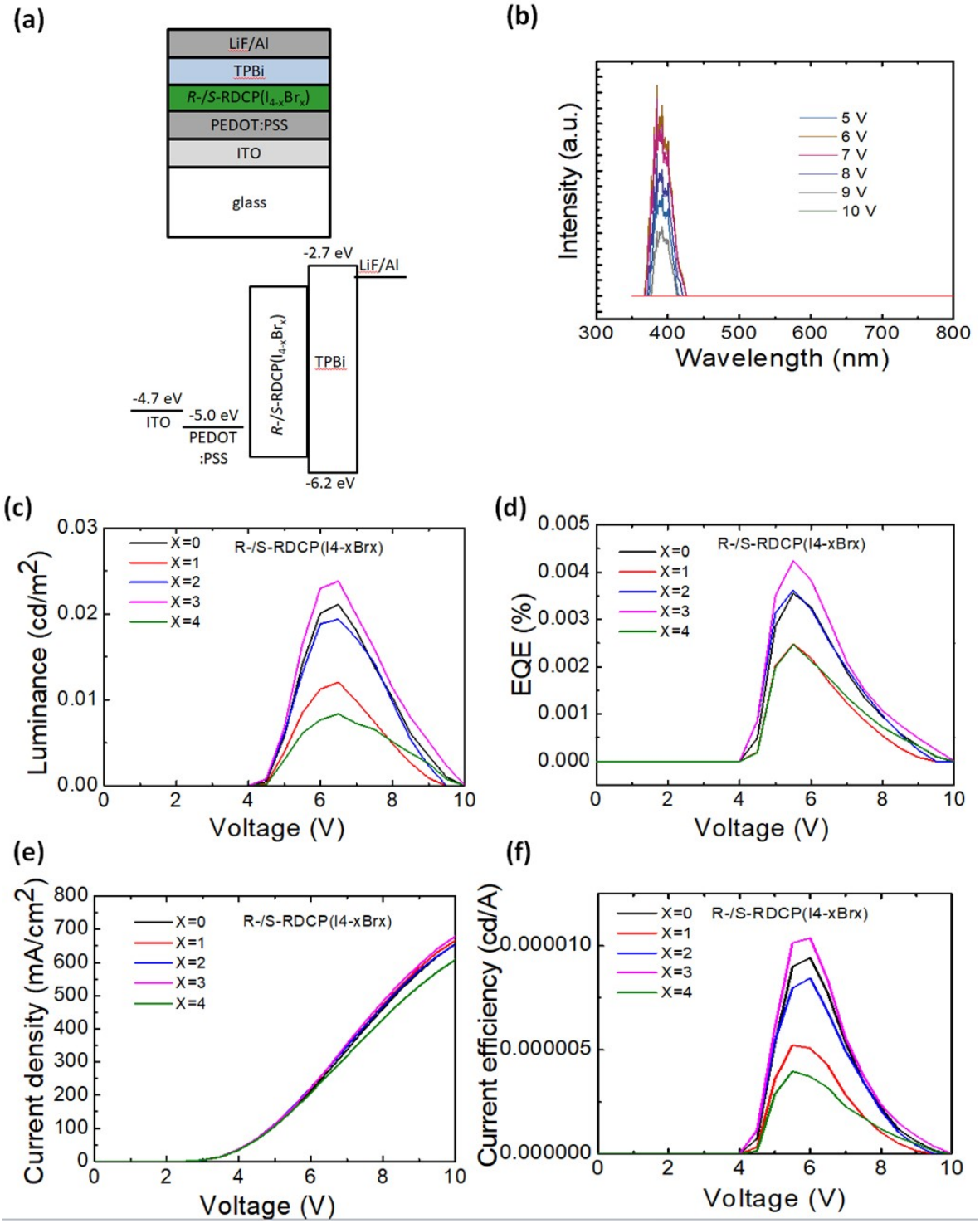

Figure S29 (a) Device structure and energy band diagram of the device without super yellow layer. (b) EL spectra for different applied voltages. (c) Luminance versus voltage, (d) EQE versus voltage, (e) current density versus voltage, and (f) current efficiency versus voltage for various halide compositions.

Table S2. Comparisons with previous works.

Spin filter	Emissive layer	EQE [%]	g_{CPEL}	Ref.
(*R*-MBA)$_2$PbI$_{4-x}$Br$_x$ (*S*-MBA)$_2$PbI$_{4-x}$Br$_x$	Super Yellow	2	+0.01 -0.01	This work
(*R*-MBA)$_2$PbI$_4$ (*S*-MBA)$_2$PbI$_4$	CsPbI$_3$/Br$_3$ NCs	10 10.5	+0.026 -0.026	[31]
	MAPbBr3 NCs with chiral perovskite shell		+-0.006	[48]
(*R*-MBA)$_2$PbI$_4$ (*S*-MBA)$_2$PbI$_4$	CdSe QDs	0.9 1	0.02 -0.005	[50]